EUROPEAN ORGANIZATION FOR NUCLEAR RESEARCH

PRECISION MEASUREMENT OF PROTON-PROTON TOTAL CROSS-SECTION AT THE CERN INTERSECTING STORAGE RINGS

U. Amaldi, G. Cocconi, A.N. Diddens*), Z. Dimčovski, R.W. Dobinson, J. Dorenbosch, P. Duinker, G. Matthiae, A.M. Thorndike**) and A.M. Wetherell

CERN, Geneva, Switzerland

G. Bellettini***), P.L. Braccini, R. Carrara, R. Castaldi†), V. Cavasinni††), F. Cervelli, T. Del Prete, P. Laurelli, M.M. Massai, M. Morganti, G. Sanguinetti, M. Valdata-Nappi and C. Vannini

Istituto di Fisica dell'Università
and Istituto Nazionale di Fisica Nucleare, Pisa, Italy

A. Baroncelli and C. Bosio

Istituto Superiore di Sanità
and Istituto Nazionale di Fisica Nucleare, Rome, Italy

G. Abshire, J. Crouch, G. Finocchiaro, P. Grannis, H. Jöstlein, R. Kephart, D. Lloyd-Owen and R. Thun†††)

State University of New York, Stony Brook, USA

Geneve - 27 June 1978

(Submitted to Nuclear Physics)

---

*) Present address: NIKHEF, Amsterdam, Holland.

**) Present address: Brookhaven National Laboratory, Upton, New York, USA.

***) Present address: Laboratori Nazionali di Frascati dell'INFN, Frascati, Italy.

†) CERN Fellow.

††) Also at Scuola Normale Superiore, Pisa, Italy.

†††) Present address: Dept. of Physics, University of Michigan, Ann Arbor, Mich., USA.

INTRODUCTION

The proton-proton total cross-section σ at the highest machine energies available nowadays was first measured in two independent experiments[1,2], performed at the CERN Intersecting Storage Rings (ISR) about three years ago by the CERN-Rome (CR) and the Pisa-Stony Brook (PSB) groups. Although the methods used by the two teams were different (the CR group in fact deduced the value of the total cross-section, via the optical theorem, from the elastic scattering in the forward region, while the PSB group directly measured the total interaction rate), both experiments had to make use of the ISR luminosity L, measured by the Van der Meer (VDM) method[3], in order to derive the absolute value of the cross-section. The two experiments agreed in observing an unexpected remarkable rise of σ with increasing energy. At that time, however, repeated luminosity calibrations were found to be consistent only within ±2% and, moreover, it was assumed that the luminosity measurements could be affected by an energy-independent error up to ±2%, due to the uncertainty of the calibration of the magnets which displace the beams vertically in the ISR during the VDM procedure. Since a systematic error on L alters the scale of the measured cross-sections in different ways in the two experiments (the σ scale depends on $\sqrt{L}$ in the CR method and on L in the PSB method), the good agreement between the results from the two groups indicated that the VDM method was not subject to large errors. However, even a direct measurement[4] of the beam displacement scale could not exclude systematic errors as large as 2%.

It was therefore felt desirable to perform new measurements of σ using a method which did not require the knowledge of L. Since the CR and the PSB methods depend differently on L, a luminosity-independent measurement can be obtained if the two experiments are performed under conditions guaranteeing that L is the same for both (for example, in the same intersection region and at the same time). In this case, in fact, the measurement of the value of L becomes superfluous and the value of σ can be determined by comparing the rate of elastic scattering in the forward direction to the total interaction rate. These arguments induced the PSB and the CR groups to join together to perform new combined σ-measurements in intersection area I8 of the ISR. It should be noted that during the last years the ISR operation has considerably improved, and that the VDM luminosity calibration is now expected[5] to be reliable to ±0.5%. In these conditions, also the separate PSB and CR measurements are expected to give more precise determinations of σ and therefore deserve a renewed interest in them.

This article is a detailed report of the new measurements of σ, whose results have already been presented elsewhere[6]. The final values differ slightly (less than 0.1%) from the ones contained in the letter of Ref. 6, because recently

measured values for the ratio ρ between the real and imaginary part of the forward elastic amplitude[7] have been used. In Section 1 of the present paper the VDM procedure for the determination of the ISR luminosity is described. The measurements of σ by the PSB and CR methods are discussed in detail in Sections 2 and 3, respectively. In Section 4 the results obtained by the luminosity-independent method are discussed, and in Section 5 brief conclusions are drawn.

1. MEASUREMENT OF THE ISR LUMINOSITY BY THE VAN DER MEER METHOD

Proton-proton collisions producing a given final state J with cross-section σ_J (cm^2) occur in an ISR intersection at a rate

$$R_J = \sigma_J \, L \ (sec^{-1}) \ . \tag{1}$$

This expression defines the luminosity L (cm^{-2} sec^{-1}) of the colliding beams at that intersection. The value of L depends only on the currents I_1 and I_2 of the two beams and on their vertical (z-axis) overlap, because in the ISR the beams cross, at a fixed angle $\alpha = 14.77°$, in the horizontal plane. If z is the distance from the centroid of each beam, and

$$I_{1,2} = \int_{-\infty}^{+\infty} i_{1,2}(z) \, dz \ , \tag{2}$$

then

$$L(\delta) = \frac{1}{K} \int_{-\infty}^{\infty} i_1(z) i_2(z + \delta) \, dz \ . \tag{3}$$

where

$$K = \beta c e^2 \, \frac{\sin \alpha/2}{\left[1 - \beta^2 \sin^2 (\alpha/2)\right]^{\frac{1}{2}}} \simeq \beta c e^2 \, \mathrm{tg} \, \frac{\alpha}{2} = \beta \ 0.9972 \times 10^{-28} \ (A^2 \ cm \ sec) \ ,$$

and $\delta = z_1 - z_2$ is the vertical displacement between the centroids z_1 and z_2 of the two beams.

To determine the value of L, a monitor consisting of two telescopes of scintillation counters placed symmetrically downstream from the intersection is employed. If the distance of the telescopes from the crossing point is large enough, a left-right coincidence between the telescopes detects only events produced in pp colliding beam interactions; the monitor coincidence rate is then, from Eqs. (1) and (3),

$$R_M(\delta) = \frac{\sigma_M}{K} \int_{-\infty}^{+\infty} i_1(z) i_2(z + \delta) \, dz \ , \tag{4}$$

where σ_M denotes the inclusive cross-section for all events triggering the monitor.

If δ is now varied in small, precise steps (by steering the ISR beams vertically), the following integral can be measured, as suggested by Van der Meer[3]:

$$\int_{-\infty}^{+\infty} R_M(\delta)\, d\delta = \frac{\sigma_M}{K} \iint i_1(z) i_2(z+\delta)\, dz\, d\delta = \frac{\sigma_M}{K} I_1 I_2 \ . \qquad (5)$$

The beam currents are measured to better than 0.1%, so that this relation leads to the determination of the monitor constant σ_M. When σ_M is known, the ISR luminosity can be deduced at any time from the counting rate of the monitor, via Eq. (1):

$$L = \frac{R_M}{\sigma_M} \ . \qquad (6)$$

During the experiment, VDM calibrations were repeated many times at each ISR energy in different beam conditions, using simultaneously four independent monitors with σ_M ranging from ~ 0.3 to ~ 25 mb. Although all these monitors gave consistent results, the most inclusive one (consisting in the coincidence of the small-angle PSB hodoscopes $H_3^L H_4^L H_3^R H_4^R$, with $\sigma_M > \frac{1}{2}\sigma$, see Section 2) was the most stable. Therefore only the calibrations obtained with this monitor were retained in the final analysis. The statistical error of each calibration was of the order of $\pm 0.2\%$. However, the dispersion of several measurements repeated for about five months was well consistent with the expected statistical fluctuations at the three lower energies only, while increasing to 0.7-0.8% at the two higher energies (see Fig. 8, full circles). This finding is in any case consistent with the estimate[5] made by ISR experts that the uncertainties in the magnet settings are such that VDM calibrations can be reproduced only within $\pm 0.5\%$. In the final analysis the dispersion of the available measurements at each energy was assumed as error on the monitor calibration, with a lower limit of 0.5%. A summary of the values adopted for σ_M and their errors is found in Table 1. It is worth mentioning that such precisions could only be attained when a number of precautions were adopted; for instance:

i) VDM calibrations in the intersection area of this experiment alone were performed, in order to avoid perturbations in the vertical beam displacements due to cross-talk between different areas;

ii) the VDM curve in each calibration was swept by constantly increasing (or decreasing) the vertical displacement δ, in order to avoid the effects of magnet hysteresis;

iii) corrections were applied in order to compensate for the difference between the actual values and the nominal values of the parameters (radial average position and width) of each ISR stack;

iv) all calibrations were performed with low-current beams ($\lesssim 4$ A) in order to minimize the number of accidental coincidences. These were subtracted from the monitor rate using time-of-flight techniques.

The above considerations refer to the relative fluctuations of separate luminosity measurements (point-to-point error). On the other hand, the absolute value of L depends linearly on the absolute value of the displacement δ. Since the energy-independent position error of the beams is estimated[5] to be about 5 μm per millimetre of displacement, it is expected that the absolute value of L, which determines the scale of the cross-section, be known within $\Delta L/L \simeq \pm 0.5\%$ (scale error). The measurements performed in this experiment have shown that indeed the errors of L are of this order of magnitude (see Section 4).

2. MEASUREMENT OF σ BY THE PISA-STONY BROOK METHOD

2.1 Experimental apparatus

The apparatus, shown in Fig. 1, was essentially the one already used by the PSB group for the previous measurement of the total cross-section. A summary description of it is given here, and more details can be found in Ref. 2. The angular region, included in two cones (referred to as "Left" and "Right" arms) of about 30° aperture around each beam downstream from the interaction region, was covered in three steps by coincidences between pairs of circular hodoscopes about one metre apart from each other. As first angular step, the coincidence between hodoscopes H_1 and H_2, set at 1.2 and 2.2 m respectively from the intersection region, detected particles produced at angles $4° \lesssim \theta \lesssim 30°$ with respect to each beam. In a similar way, the coincidence between H_3 and H_4, which were set at 6.5 and 7.5 m respectively from the crossing point, covered angles between $\sim 0.8°$ and $\sim 7°$. Finally, the third angular step was covered by the coincidence of two small hodoscopes TB_1 and TB_2, positioned about 9 m from the intersection region, where the cylindrical vacuum pipe had narrowed to an elliptical cross-section. This last step was important to recover a large fraction of elastically or quasi-elastically scattered protons, which are strongly collimated in the forward direction. In the horizontal plane, in fact, particles scattered at angles down to ~ 8 mrad could be detected, and in the vertical plane angles as small as 3 mrad were covered. A large-angle detector (L-box) surrounded the interaction region and covered angles larger than 40° with respect to either beam. It consisted of four planes of counters, each one used in coincidence with one of four small counters L_s (not shown in Fig. 1) mounted close to the wall of the beam vacuum pipe in the intersection region.

Over the whole solid angle covered by the trigger hodoscopes, additional hodoscopes finely split into bins of polar angle detected the multiplicity and the angular distribution of the charged secondaries. This information was used to estimate the fraction of inelastic events lost by the trigger (see Section 2.6).

2.2 Data taking

The great majority of pp interactions were detected by the coincidence between the Left and the Right arm. A small fraction of events, however, gave tracks in only one of the two arms and in the region around 90°. In order to detect these events (referred to as L-triggers in the following) use was made of the coincidence between the four $(L \cdot L_s)$ signals, OR-ed together, and the signal produced by the Left arm. Owing to the left-right symmetry of the apparatus, the number of events which triggered this coincidence, but did not trigger the Left-Right coincidence, had to be counted twice. The data acquisition was triggered by the following logical signal:

$$T = \left\{(H_1 \cdot H_2) + (H_3 \cdot H_4) + (TB_1 \cdot TB_2)\right\}_{Left}$$

$$\times \left\{\left[(H_1 \cdot H_2) + (H_3 \cdot H_4) + (TB_1 \cdot TB_2)\right]_{Right} + (L \cdot L_s)\right\} .$$

When a trigger occurred, all information pertinent to the event was transferred to an on-line computer via a CAMAC system. This information included a pattern-unit bit (fired or not fired) for each counter of the hodoscopes, clock readings of the live time of the experiment, and seven digitized time-of-flight (TOF) differences between the triggering signal and the signals from each hodoscope. The operating conditions of the apparatus and of the electronics were continuously checked by the on-line computer during the data acquisition runs. A high-speed light-emitting diode (LED) was stuck on each counter in order to be able to simulate the passage of a particle through the counter. The timing of the pulses coming from the LEDs was frequently checked to be constant within ±1 nsec, and the driver pulses lighting the diodes were adjusted to give about the same pulse height as for minimum ionizing particles. The firing of the LEDs was computer-controlled and allowed the simulation of any event configuration. With this technique the rate of trigger losses due to dead-time could be measured (see Section 2.5). Data were taken with low-current stacks (2 to 5 A in each ISR beam) yielding beam-beam collision rates of a few thousand per second, about one hundred times lower than the usual ones at the ISR. In these conditions the level of accidentals was very low, while the beam-beam signal was still much higher than the single-beam background.

2.3 Time-of-flight distributions

Events due to beam-beam collisions were recorded together with events due to interactions of a single beam with the residual gas in the pipes or with the pipe walls. Single-beam events produced upstream of the intersection region generated

jets of secondary particles which could hit the hodoscope system. In this case, however, hodoscopes in the two arms of the apparatus were not fired simultaneously as they were for beam-beam events. The amount of time shift between the Left and Right signals depended on the distance of the various hodoscopes from the intersection region: in some cases it was large enough to produce no trigger; otherwise it could be distinguished in a time-of-flight distribution. The resolving time of the trigger coincidence was kept rather wide, ±30 nsec, and the background events accepted by the trigger were rejected by an accurate off-line analysis of the TOF distributions. Using the information of the timings of the signals from each individual hodoscope with respect to the triggering signal, all 12 TOFs between hodoscopes in the Left arm and hodoscopes in the Right arm were computed by difference.

Because of the high mean multiplicity of secondary particles, the great majority of events appeared simultaneously in more than one TOF spectrum. To avoid double counting, "reduced" TOF distributions were defined in such a way that each event appeared only in one TOF: after having assigned priorities to the 12 TOFs, each event was displayed only in the fired TOF with highest priority. The TOF spectra involving only hodoscopes H_4 and TB showed a beam-beam peak alone and no single-beam background, these hodoscopes being far enough from the intersection region to allow rejecting single-beam events at the trigger level. The TOFs between any hodoscope at Left and H_2^{Right} showed an accumulation of events due to beam-1 interactions at shorter times than the beam-beam events. Analogously, the TOFs between H_2^{Left} and any hodoscope at Right showed an accumulation of beam-2 events on the right of the beam-beam peak. Owing to the particular configuration of the trigger, the TOFs between any hodoscope of the Left arm and the L-box had the peculiarity that the beam-1 background lay below the beam-beam peak; beam-2 background, instead, gave a bump on the right of the beam-beam peak in TOF H_2^{Left}-L and was outside the trigger acceptance in TOFs TB^{Left}-L and H_4^{Left}-L.

2.4 Background subtraction

In addition to single-beam peaks, all TOFs showed a flat background, of the order of 1% of the sample, due both to accidental left-right coincidences and to good events whose TOF value had been randomly displaced by an out-of-time start or stop in the TOF electronic chain. In the analysis the flat background was first removed from the TOF distributions, as explained in detail below, and the good events with time shift due to an accidental count were rescued in special test runs ("echo runs") described in Section 2.5. The various TOFs were treated in three different ways, according to their features:

i) In the TOFs free from single-beam contamination (i.e. H_4^L-H_4^R, H_4^L-TB^R, TB^L-H_4^R, TB^L-TB^R, gathering from 60% to 90% of the events, depending on the energy)

the flat background was subtracted from the beam-beam peaks by extrapolating the level observed in the region of the spectrum away from the peaks. The events remaining inside some fiducial cuts after this subtraction were accepted as good beam-beam events.

ii) For the TOFs showing single-beam peaks (i.e. H_4^L-H_2^R, TB^L-H_2^R, H_2^L-H_4^R, H_2^L-TB^R, H_2^L-H_2^R, gathering from 40% to 10% of the events) the shape of the background peak, as obtained in separate runs with only one beam circulating in the ISR, was added to a constant level with a free relative normalization, fitted to the TOF distribution in the region outside the beam-beam peak, and then subtracted from the spectrum. Here again, the events falling in the beam-beam peak within some fiducial cuts were accepted as good events. Although these fits were performed separately on each TOF, the normalization factors between the single-beam runs and the beam-beam run obtained by the fit to TOF H_2^L-H_2^R (where both single-beam peaks are present) were found to agree to those obtained by the fits to TOFs H_4^L-H_2^R and TB^L-H_2^R (containing a beam-1 background peak only) and to TOFs H_2^L-H_4^R and H_2^L-TB^R (which contain a beam-2 background peak only).

iii) In the TOFs involving the L-box (i.e. H_4^L-L, TB^L-L, H_2^L-L, gathering from 4% to 1% of the events) the beam-1 background which lay below the beam-beam peak was subtracted using the average normalization factor found by the previous fits. This was done after having subtracted the flat background from TOFs H_4^L-L and TB^L-L as in (i) and the beam-2 plus the flat background from TOF H_2^L-L as in (ii).

It may be noticed that, since each event might appear in several TOFs at the same time, the population of events in each "reduced" TOF strongly depended on the chosen sequence of priorities: the high-priority TOFs were the richest, regardless of the hodoscopes involved, while very few events were left in the low-priority TOFs. In order to minimize systematic errors which could have been committed in the fit and in the subtraction of single-beam background, in the final analysis a lower priority was assigned to the TOFs more contaminated by single-beam events. In particular, TOF H_2^L-H_2^R, from which both beam-1 and beam-2 background had to be subtracted, was given a low priority. It was followed only by the TOFs involving the L-box, in which the subtraction of beam-1 background, lying under the beam-beam peak, was indirect since it was based on a normalization derived from the fits to the other TOF spectra.

In addition to accidental counts, there was another effect which caused some good events to be observed with a time shift in some TOF distributions. This was due to delayed tracks, correlated with the event itself. For example, it was found that in a fraction of elastic events (up to 5% at the highest energy), one

of the scattered protons after crossing the TB counters interacted with the iron of the ISR magnet behind, yielding slow backward prongs which fired H_4^R (H_4^L) with some variable delay with respect to TB^R (TB^L). Two TOFs were thus available, TB^L-TB^R with the right value and $TB^L-H_4^R$ ($TB^R-H_4^L$) with a displaced value. Such an event would either be accepted or rejected according to which one of the two TOFs had higher priority. In general, when delayed tracks are correlated to a good event, this can be lost in the analysis with a probability which depends on the particular choice of priorities. The amount of such a loss, reaching 1% in the worst case, is illustrated by columns 3 and 4 of Table 2, which show the results obtained with two different sequences of priorities in a typical run at $\sqrt{s}$ = 62.7 GeV, where the effect is maximum. This difficulty was overcome in a final analysis in which the sequence of TOF priorities was not fixed, in the sense that a lower-priority TOF could prevail over a higher-priority TOF if the value of the time-of-flight was inside some tight beam-beam cuts in the former and outside the beam-beam peak in the latter*). With this method, identical final results were obtained with two different sequences, as shown in columns 1 and 2 of Table 2. The percentage of rescued events was found to be completely insensitive to the features of the particular ISR stack. The energy-dependence of the partial contributions of the various TOFs is illustrated in Table 3.

2.5 Estimate of randoms

The probability for good events to show a randomly displaced TOF value was measured in special test runs. In these runs, taken immediately after the normal beam-beam runs, the LED system was operated by the on-line computer in the following way. When a trigger occurred, the configuration of the counters hit in the event was read from the pattern units and recorded on magnetic tape with a flag specifying that it was a "true" event. The same configuration was then written on output registers and the corresponding LEDs were accordingly fired. If no dead-time prevented the trigger from being fired, a new event resulted, with a configuration identical to the previous one and with a good TOF value in the absence of accidental counts. This "echo" event was in turn read and recorded on magnetic tape with another flag. The tape was subsequently analysed off-line, retaining only the "echo" events associated with true events whose TOF fell inside beam-beam cuts. The number of events to be rescued in the analysis was obtained from the fraction of "echo" events rejected by the same computer program used to

*) Some restrictions were, however, imposed in order to avoid such changes of priorities causing distortions in the shape of the single-beam background. In fact, single-beam events with a TOF value falling near a cut could generate an accumulation of background inside and a depletion outside the cut, in the neighbourhood of the cut itself. Therefore, TOFs contaminated by single-beam background were allowed to prevail only over TOFs free from single beams. Moreover, the TOFs involving the L-box were left at fixed priorities. It was checked that the final result was insensitive to the precise location of the cuts.

analyse the corresponding beam-beam run. In addition, the trigger losses due to electronic dead-time were measured by the fraction of "echo" events which failed to fire the trigger and were rarely found to exceed 0.1%. The fraction of rescued events ranged from 0.1% to 0.4% of the total, depending on the quality of the stack. It was checked over the whole running period of the experiment that the trigger failures due to inefficiencies of the LED system were negligible. This test was made immediately after each ISR stack, and consisted of "echoing" beam-beam events, read from a magnetic tape, when no beams were circulating in the ISR.

2.6 Corrections

The slightly incomplete coverage of the solid angle made the rates measured in the PSB detector smaller than the total interaction rate, and corrections had to be introduced to compensate for the events not accepted by the trigger. Most of the non-covered solid angle was concentrated in the two coronas between $\theta = 30°$ and $\theta = 40°$, i.e. in the gaps between hodoscopes $H_2^{L,R}$ and L. The probability of an event in which all charged particles emitted in one hemisphere fell in such a gap was evaluated by extrapolating the θ-dependence of the L-triggers. Such a loss was found not to exceed 0.1% at all energies and it was neglected. The probability that all charged particles of an event were emitted only at angles larger than 30° in both hemispheres turned out to be negligible too. Also completely negligible was the effect of the upstream holes in hodoscopes $H_2^{L,R}$. Important losses, on the contrary, were due to small-angle processes escaping the trigger because of the beam exit holes in TB hodoscopes, at $\theta \lesssim 5$ mrad. In addition, a non-negligible fraction of events was lost by the trigger because of the dead space between adjacent trigger counters.

2.6.1 Elastic loss at small angles

The loss of elastic events in which at least one proton was scattered within the inner edge of the TB counters was computed by a Monte Carlo calculation simulating the production of elastic events over the beam-beam overlap region according to data previously measured[8] at the ISR. The absolute value of this correction was computed, while the other losses discussed below were evaluated as ratios to the measured rate. A summary of the input data and of the elastic correction computed at each energy is given in Table 4. The error of the input parameters and the indetermination due to edge effects in the hole inside the TB counters have about equal weight on the uncertainty of the correction. At the highest energies, this uncertainty is not negligible with respect to the other sources of error. It is worth mentioning that the losses listed in Table 4 include a negative correction which compensates for Coulomb scattering, which was appreciable because elastic events with protons scattered in the vertical plane at angles as small as 3 mrad could trigger the apparatus. The increase of measured cross-section due to

this effect was also computed by a Monte Carlo method, using the known Coulomb cross-section as an input. It amounted to 0.12 and 0.07 mb at p_{ISR} = 11 and 15 GeV/c, respectively, and was negligible at higher energies.

2.6.2 Inelastic loss at small angles

The loss of inelastic events at small angles was evaluated in the following way. All events triggering the coincidence between the Left and the Right arm independently of the L-box (i.e. all events except the L-triggers, see Section 2.2) were plotted in a two-dimensional graph, as sketched in Fig. 2, whose axes were the maximum angle of the prongs emitted in the left and in the right hemisphere. In such a plot, a narrow band 5 mrad wide, corresponding to the pipe exit holes, is empty and its contribution must be evaluated by extrapolating the distribution of the events plotted in the graph. The extrapolation of the L-triggers was neglected owing to the smallness of the contribution of the L-triggers themselves. Three classes of events could be distinguished, as shown in Fig. 2. Class I contained the events with no track in hodoscopes $H_2^{L,R}$ and L; Class II the events with no track in the L-box and with at least one track in hodoscopes H_2^L or H_2^R; Class III the events with tracks in the Left cone, in the Right cone, and in the L-box. The extrapolation of Class III could only lead to the determination of a fraction of "L-trigger" events: it was not performed, since the whole category of L-triggers was directly measured by the complete trigger including the L-box (see Section 2.2). Class I included many elastic events concentrated in a narrow peak, along the diagonal of the matrix, superimposed on a smooth background. It was found that the measured rate of Class I events exceeded only by $\lesssim 4\%$ the rate of elastic events expected by a Monte Carlo calculation. This indicated that the smooth background in this region was mostly due to elastic events in which one of the scattered protons had undergone a secondary interaction in the pipe walls. Indeed, the rate of these events was consistent with the computed probability of interaction ($\sim 15\%$) for protons at these angles. Inelastic events in Class I were therefore estimated not to exceed 0.3 mb and their extrapolation was neglected. As a conclusion, only the extrapolation of Class II events had to be taken into account. The maximum-angle distribution $(dN/d\Omega)(\theta_{max})$ for these events, shown in Fig. 3, was well fitted by an exponential function of θ_{max}. The integration of this curve over the missing solid angle allowed determination of the fraction of inelastic events lost because of the TB holes. A summary of the corrections computed at each energy is given in Table 5.

2.6.3 Dead-space loss

An additional loss of elastic or inelastic events was due to the dead space in the cones covered by the trigger counters, each gap between adjacent counters being responsible for some small inefficiency in particle detection. For the

majority of inelastic events such inefficiency did not affect the trigger inclusiveness, because of the high mean multiplicity of secondary particles. A minority of inelastic events, however, amounting to about 10% of the total cross-section detected by the apparatus, showed configurations with only one track in one of the two arms, concentrated in a narrow cone of $\sim 4^\circ$ aperture (i.e. in hodoscopes $H_{3,4}$ and $TB_{1,2}$ essentially), no track in the L-box, and some tracks in the other arm. Owing to this category of events, if the coincidences $(H_3 \cdot H_4)$ and $(TB_1 \cdot TB_2)$ were affected by an inefficiency of $\alpha\%$, a fraction $0.1\alpha\%$ of σ would be lost by the trigger. In addition, elastic events, which amount to $\sim 15\%$ of the detected cross-section, would have a probability $2\alpha\%$ to miss the trigger, implying an additional loss of $0.3\alpha\%$ of σ. The total trigger inefficiency would thus be $0.4\alpha\%$: realistic values of α can therefore give rise to non-negligible losses of rate. In order to evaluate the trigger inefficiency due to dead space, special runs were taken with the coincidences $(H_3 \cdot H_4)$ and $(TB_1 \cdot TB_2)$ operating in singles in one of the two arms. In these runs the trigger logic was thus modified as follows:

$$T' = \left\{(H_1 \cdot H_2) + (H_3 \cdot H_4) + (TB_1 \cdot TB_2)\right\}_{Left}$$

$$\times \left\{\left[(H_1 \cdot H_2) + H_3 + H_4 + TB_1 + TB_2\right]_{Right} + (L \cdot L_s)\right\}$$

or, alternatively, with the ORs at the Left side. Actually, one should have taken data with the ORs in both sides at the same time, but this usually introduced too high an amount of background. On the other hand, it was checked in some particular cases that the correction measured with the ORs in both sides exceeded by no more than a few percent the sum of the corrections measured with the ORs in either side. By making use of the information of the pattern unit bits, only the events satisfying trigger T′, but not trigger T, were selected off-line. These events, displayed in TOF distributions, showed a clear peak at the same position as the beam-beam peak in normal runs, as illustrated in Fig. 4. Most of the beam-beam signal came from TOF TB^L-TB^R; less important but neat signals were present in TOFs H_4^L-TB^R, TB^L-H_4^R, and H_4^L-H_4^R; no signal at all was observed in the other TOFs. For each run taken with trigger T′, it was checked that the pattern units were not affected by any inefficiency which could simulate such a loss. This test was made by applying the analysis described above to normal trigger runs taken immediately after each T′ run. It was also checked that such a loss was not due to electronic dead-time. In fact the fraction of "echo" events (see Section 2.5) which failed to fire the trigger was never found to exceed 0.15%. The losses measured at each energy with this method (from 1.1% to 1.5%) are consistent with what can be expected from the size of the gaps between adjacent counters, and are summarized in Table 6.

2.7 Results

The total cross-section in the PSB method was obtained by the following expression:

$$\sigma = \sigma_M \frac{R}{R_M} (1 + \varepsilon) + \Delta\sigma_{el} \ , \tag{7}$$

where the luminosity L has been expressed as the ratio of R_M to σ_M [Eq. (6)], R is the rate of beam-beam events (corrected for randoms) measured by the PSB apparatus, $\Delta\sigma_{el}$ the small-angle loss of elastic cross-section listed in Table 4, and ε the global inefficiency of the trigger due to both inelastic loss at small angles (Table 5) and dead-space losses (Table 6). Figure 8 shows all the measurements of σ_M and of the ratio R_M/R performed during the period of data taking. The values finally obtained for σ with the PSB method are summarized in Table 7.

3. MEASUREMENT OF σ BY THE CERN-ROME METHOD

3.1 The method

The total cross-section is related to the elastic hadronic cross-section in the forward direction through the optical theorem. Neglecting spin effects we can write:

$$\sigma = \frac{4\pi}{p} \sqrt{\frac{1}{1 + \rho^2} \left.\frac{d\sigma^{hadr}}{d\Omega_{cm}}\right|_{t=0}} \ , \tag{8}$$

where p is the c.m. momentum and ρ is the ratio of the real to the imaginary part of the forward elastic scattering amplitude. At ISR energies, ρ is positive and of the order of a few percent[7]. Since the detector of elastically scattered protons is set at some angle with respect to the unscattered beam, the forward cross-section appearing in Eq. (8) is obtained by extrapolating to $t = 0$ the one measured at some momentum transfer t_0. Assuming that the elastic differential cross-section in the region $0 < |t| < |t_0|$ is an exponential function of t with slope b, Eq. (8) can be rewritten as

$$\sigma = \frac{4\pi}{p} \sqrt{\frac{1}{1 + \rho^2} e^{b|t_0|} \left.\frac{d\sigma^{hadr}}{d\Omega_{cm}}\right|_{t=t_0}} \ . \tag{9}$$

In order that the extrapolation to $t = 0$ be reliable, it is necessary that the detector measures elastic scattering at very small angles, where both hadronic and Coulomb amplitudes contribute to the elastic differential cross-section:

$$\frac{d\sigma^{meas}}{d\Omega} = \left| f^{hadr} + f^{Coul} \right|^2 \ . \tag{10}$$

Assuming that the real and the imaginary part of the hadronic amplitude have the same t-dependence (i.e. that ρ = Re f^{hadr}/Im f^{hadr} is independent of t), f^{hadr} can be written as:

$$f^{hadr} = \frac{p}{4\pi} \sigma \, (\rho + i) \exp\left(-\frac{b}{2} |t|\right) . \tag{11}$$

The Coulomb amplitude f^{Coul} can be parametrized in the following form[9]:

$$f^{Coul} = -2\alpha p \frac{G^2(t)}{|t|} e^{i\alpha\phi} , \tag{12}$$

where α is the fine structure constant, G(t) is the proton electromagnetic form factor

$$G(t) \simeq 1 - 2.94 \, |t| , \tag{13}$$

and ϕ is a phase factor[10]

$$\phi = \ln \frac{0.08 \ (\text{GeV/c})^2}{|t|} - 0.577 . \tag{14}$$

As a result, the elastic differential cross-section measured by the detector exceeds the hadronic cross-section by the fraction ε_C (due to Coulomb scattering) and ε_I (due to the interference between the Coulomb and the hadronic amplitudes) defined by the following expressions:

$$\frac{d\sigma^{meas}}{d\Omega} = \frac{d\sigma^{hadr}}{d\Omega} \left(1 + \varepsilon_C + \varepsilon_I\right) , \tag{15}$$

$$\varepsilon_C = 64\pi^2\alpha^2 \frac{G^4(t)}{|t|^2} \frac{e^{b|t|}}{\sigma^2(1 + \rho^2)} , \tag{16}$$

$$\varepsilon_I = -16\pi\alpha \frac{G^2(t)}{|t|} \frac{\rho + \alpha\phi}{\sigma(1 + \rho^2)} \exp\left(\frac{b}{2} |t|\right) . \tag{17}$$

The elastic differential cross-section is measured by the rate R_{el} of elastic events in a detector covering a solid angle $\Delta\omega$:

$$\frac{d\sigma^{meas}}{d\Omega} = \frac{R^{el}}{\Delta\omega} \frac{1}{L} . \tag{18}$$

Combining Eqs. (9), (15), and (18), the total cross-section σ can finally be expressed in terms of the measured quantities as follows:

$$\sigma = \sqrt{\frac{16\pi^2}{p^2} \frac{1}{1 + \rho^2} \frac{1}{1 + \varepsilon_C + \varepsilon_I} e^{b|t_0|} \frac{R^{el}}{\Delta\omega} \frac{1}{L}} = \sqrt{\frac{F}{R_M} \sigma_M} , \tag{19}$$

where the last equation is the definition of the quantity F, and the luminosity L has been expressed as the ratio of R_M to σ_M [Eq. (6)].

3.2 Apparatus

Elastic events were detected by two symmetric sets of hodoscopes A and B, sketched in Fig. 1, covering angles from 3 to 9 mrad. Each hodoscope consisted of two separate arrays of 12 horizontal and 11 vertical scintillation counters. The horizontal scintillators (called θ_1, ..., θ_{12}) were 4.5 mm wide and 90 mm long, while the vertical scintillators (called ϕ_1, ..., ϕ_{11}) were 8 mm wide and 80 mm long. Each hodoscope was placed between two trigger counters (A'A" and B'B"). Hodoscope A (B) was held fixed at a distance of 28 mm above (below) the circulating proton beams, situated in an indentation in the ISR vacuum pipe that permitted the protons scattered in the vertical plane to reach the hodoscope after crossing a stainless-steel wall no more than 1 mm thick.

The fourfold coincidence A'A"B'B" was used to initiate the data acquisition system. For each event, the pulse heights of all counters in hodoscopes A and B were measured, as well as the time-of-flight differences between the triggering signal and the trigger counters (including the PSB hodoscopes). The status (fired or not fired) of each counter was registered in pattern units. In addition, the live time before each event was measured by a high-frequency clock. Each piece of information was then transferred, via a CAMAC system, to an on-line computer which also monitored the performances of the apparatus and wrote all information on magnetic tape.

3.3 Data reduction

Elastic scattering events dominated the AB coincidence. Thus, choosing an element ω_{ij} (defined as the intersection of counter θ_i with counter ϕ_j) in hodoscope B, the distribution of hits in hodoscope A showed (superimposed on a low inelastic background) a sharp bi-dimensional almost Gaussian peak corresponding to the shadow of the interaction diamond projected on A from the element chosen in B (see Fig. 5a). In the analysis such an element was chosen out of the central "window" of 4 × 5 elements in hodoscope B. In order to evaluate the volume of the elastic peak, a fiducial region PK of 5 × 7 = 35 elements was defined in hodoscope A, centred on the peak, as shown in Fig. 5b. Since the inelastic background did not show any evident ϕ-dependence, its level was evaluated in the regions L and M (4 elements for each θ-bin, 20 elements over-all, see Fig. 5b) and interpolated into the region PK. Such an evaluation was effected, after having fitted the shape of the elastic peak, by computing the difference between the number of events observed in L+M and the number of events expected by the fit. In more detail, the number of coincidences $N_{ij,k\ell}$ between the element (i,j) of hodoscope B and the element (k,ℓ) of hodoscope A was expressed as the sum of a term E fitted to the elastic peak and an inelastic contribution I in the following way:

$$N_{ij,k\ell} = E_{ij,k\ell} + I_{ij,k\ell} \,, \tag{20}$$

where

$$I_{ij,k\ell} = \frac{1}{4} \sum_{\lambda \in L,M} \left(N_{ij,k\lambda} - E_{ij,k\lambda} \right) . \tag{21}$$

The fit consisted in parametrizing the shape of the diamond by an analytical function. The transverse distributions of interaction points in the diamond, as well in the vertical direction z as in the radial direction y, were parametrized by means of properly normalized Breit-Wigner functions with variable exponent:

$$f(z) \propto \left[1 + \left(2^{1/\mu} - 1 \right) \left(\frac{z - z_0}{\delta} \right)^2 \right]^{-\mu} \tag{22}$$

$$g(y) \propto \left[1 + \left(2^{1/\nu} - 1 \right) \left(\frac{y - y_0}{\eta} \right)^2 \right]^{-\nu} . \tag{23}$$

These functions have tails which are higher than for a Gaussian distribution, and they tend to Gaussians for large values of the exponents. The elastic peak $E_{ij,k\ell}$ was then computed as a function of the density of the source (see Fig. 6):

$$E_{ij,k\ell} = \tilde{L} \int \frac{d\sigma}{d\Omega} f(z)\, dz\, g(y)\, dy \frac{dy_1 dz_1}{d_1^2} \frac{dy_2 dz_2}{d_2^2} \delta(\alpha_1 - \alpha_2)\, \delta(\beta_1 - \beta_2) \,. \tag{24}$$

In Eq. (24) $\tilde{L}$ is the luminosity integrated over the time of data taking and $d\sigma/d\Omega$ is the cross-section of Eq. (10). The meaning of the other symbols is clarified by inspection of Fig. 6. The factors $\delta(\alpha_1 - \alpha_2)$ and $\delta(\beta_1 - \beta_2)$ express the conditions of coplanarity and angular correlation satisfied by elastic events. Integration of Eq. (24) leads to

$$E_{ij,k\ell} = \tilde{L} \left. \frac{d\sigma}{d\Omega} \right|_{\theta = \theta_{ij,k\ell}} \frac{wh}{\left(\frac{d_1 + d_2}{2} \right)^2} \left[f(\bar{z})\, \frac{h}{2} \right] \left[g(\bar{y})\, \frac{w}{2} \right] , \tag{25}$$

where $\theta_{ij,k\ell}$ is the scattering angle defined by the centres of the two elements (i,j) and (k,ℓ) and the direction of the initial protons.

A fit to 700 independent counting rates $N_{ij,k\ell}$ ($i = 1, \ldots, 4$, $j = 1, \ldots, 5$; $k = 1, \ldots, 5$, $\ell = 1, \ldots, 7$) was then performed with the following six free parameters*):

---

*) $\tilde{L}$ has not to be regarded as a free parameter because of the normalization condition

$$\sum_{i,j,k,\ell} N_{ij,k\ell} = N_{tot} \,,$$

where N_{tot} is the total number of events.

δ vertical half-width of the source

z_0 vertical displacement of the source

μ exponent of the vertical distribution

η radial half-width of the source

y_0 radial displacement of the source

ν exponent of the radial distribution.

For each element (i,j) of hodoscope B, the fit allowed the determination of the background-to-signal ratio BG_{ij} in the fiducial area PK of hodoscope A and the fraction BD_{ij} of elastic peak falling outside the border of area PK. The elastic rate R^{el}_{ij} detected by the element (i,j) was then expressed by

$$R^{el}_{ij} = \left[\sum_{k,\ell \in PK} N_{ij,k\ell} \right] (1 - BG_{ij}) \; (1 + BD_{ij}) \; . \qquad (26)$$

It should be stressed that the complicated fitting procedure described above is only used to compute the small correction terms BG_{ij} and BD_{ij}.

Twenty independent rates of elastic events, detected by twenty different elements of hodoscope B, were measured and, inserted in Eq. (19), led to twenty independent evaluations of the total cross-section. These values were always found to agree, within the statistical errors. As a check, the same data were also treated in the symmetric way, i.e. choosing a window of 20 elements in hodoscope A and looking at the elastic peak in hodoscope B. No systematic discrepancies in the results of the two treatments were ever found. The values of the border loss BD were kept small (from 0.4% to 4% according to the parameters of the stack of the ISR beams) by taking all data with the ISR working in the Terwilliger scheme[11]. In these operating conditions, the transverse dimensions of the diamond were particularly small ($\sim$ 1.5 mm in the vertical and $\sim$ 3 mm in the radial direction) and the width of the elastic peak was much smaller than the dimension of the hodoscope (see Fig. 7). Typical values of the background BG integrated on the area PK, ranged from 3% to 6%, depending on the energy, which corresponds to a signal-to-background ratio at the peak of more than 200:1. In the final analysis, the large hodoscopes of the PSB apparatus were used in anticoincidence to veto inelastic events. In these conditions the background was always less than 3%, approximately constant at all energies.

A particularly delicate problem was presented by those events in which more than one particle was detected in a hodoscope. One origin of multiple hits was inelastic events yielding two or more charged secondaries in one of the hodoscopes. Another origin, particularly important in these miniature scintillators, was the presence of δ-rays, created in the hodoscope itself, which could fire other counters in the neighbourhood of the main track and create ambiguities about the location of the elastically scattered proton. Three different criteria to overcome

this difficulty were tried and found to give equivalent results. In the final analysis, multiple-hit events were handled by selecting in each hodoscope the one θ and the one ϕ counter that gave a pulse with amplitude nearest to the average amplitude (best-pulse-height criterion). Alternative criteria consisted in choosing the counter with largest amplitude (maximum-pulse-height criterion) or in assigning a fraction of event to each fired counter (equal-weight criterion). All criteria led to determinations of σ which were consistent within 0.3%. An additional check consisted in ignoring the counters with pulse height less than ε% of the average, in order to cut off the majority of δ-rays, which gave very small pulse heights. The values of σ derived in this way varied by less than 0.2% by varying ε up to 20%. In the final analysis a cut at ε = 10% was applied, which gave a percentage of single-hit events in each hodoscope of $\sim$ 80%.

3.4 Corrections, errors, and results

The uncertainties of the various factors appearing in expression (19) are summarized in the following.

i) *Measurement of luminosity L.* Estimates of the errors of the monitor calibrations at each energy have been evaluated by studying the reproducibility of several repeated measurements, using the method already discussed in Section 1. An estimate of a possible energy-independent scale error will be given in Section 5.

ii) *Measurement of the elastic peak PK.* Based on the tests discussed in Section 3.3, it was estimated that the integral of the elastic peak PK might be affected by a point-to-point error (i.e. applicable to each energy independently) of ±0.5%, and by a scale error (i.e. common to all energies) up to ±0.3%.

iii) *Subtraction of background BG.* As discussed in Section 3.3, the integrated background BG under the elastic peak PK amounted to less than 3% of PK. In order to take into account some possible unexpected shape for the background under the peak, a safe margin of error was adopted assuming a point-to-point error of ±25% and a scale error of ±10% on BG.

iv) *Border loss BD.* The values of the border loss BD depended on the particular stack conditions, and a different correction was therefore applied for each run. As a matter of fact, different stacks at the same energy were often found to have similar parameters, so that this correction was empirically found to be maximum at p_{ISR} = 15 GeV/c (BD $\simeq$ 4.5%) and minimum at p_{ISR} = 22 and 26 GeV/c (BD $\simeq$ 0.5%). In order to take into account possible systematic errors in the fit on which the determination of BD is based, a generous point-to-point error of ±25% was assumed on BD.

v) *Solid angle $\Delta\omega$.* Since the width of each hodoscope strip was known with an accuracy of ±0.01 mm, the uncertainty on the solid angle $\Delta\omega$ covered by a single hodoscope element was $\Delta(\Delta\omega)/\Delta\omega = \pm 0.35\%$. However, since in the experiment the information from 40 different elements was used, the uncertainty on the average solid angle was $\{[\Delta(\Delta\omega)]/\Delta\omega\}_{av.} \simeq 0.05\%$. This was much smaller than the uncertainty of edge effects on each element. In fact, adjacent strips in each hodoscope were separated by an aluminized mylar foil 0.025 mm thick, and particles going through the dead space between two counters had a good chance of being detected by δ-ray emission. We can consider the two extreme possibilities in which the edge effect is zero or maximum. Zero edge effect would imply a dead space of (0.87 ± 0.1)% in each hodoscope. This dead space would lower the sum of the rates of the elements of indices k,ℓ [Eq. (26)], and the corresponding elastic cross-section would therefore be lower than the true one by 0.87%. Maximum edge effect would imply no dead space, but in this case the effective solid angle of the element i,j would be increased by 0.87% with respect to the geometrical value: the elastic cross-section derived in this way would be higher than the true one by 0.87%. We can thus set an upper limit of ±0.87% on the uncertainty of $\Delta\omega$. On an experimental basis, the effective dead space could be estimated by looking at the fraction of events with no hit in one of the two planes of a hodoscope, which turned out to be 0.30 ± 0.12%. This implied that the edge effects made the effective solid angle higher than the geometrical one by (0.87 ± 0.1)% - (0.3 ± 0.12)% = (0.57 ± 0.16)%. The elastic cross-section computed with the geometrical solid angle should therefore be increased by (0.57 ± 0.16)% owing to the holes on the opposite side of the element i,j, and should be decreased by (0.30 ± 0.12)% because of the underestimation of the solid angle of the same element. The elastic cross-section should then be corrected by (0.27 ± 0.26)% and the corresponding value of the total cross-section by 0.13 ± 0.13%. Owing to the smallness of the effect and to the uncertainty attached to it, no correction was actually applied to the data and an increased error was attributed to the value of the solid angle: $\Delta(\Delta\omega)/\Delta\omega = \pm 0.3\%$. This systematic error was of course common at all energies, and it generated a scale error on the final values of σ.

vi) *Extrapolation factor $F = e^{b|t|}$.* The adopted values of the slope b of the differential elastic cross-section at each energy have been deduced from the available experimental data[8] by means of a fit linear in ln s. The estimated uncertainty was $\Delta b = \pm 0.3$ (GeV/c)$^{-2}$. Several sources of error affected the determination of the momentum transfer t:

$\Delta t/t = \pm 0.2\%$ due to the uncertainty of the value of the mean ISR momentum;

$= \pm 0.08\%$ to 0.16% depending on the energy, due to the uncertainty of the initial direction of the protons in the horizontal plane;

$= \pm 0.7\%$ to 1.0% same as above, in the vertical plane;

$= \pm 0.25\%$ to 0.35% due to the uncertainty of the position of the hodoscopes.

As a whole, the global error on the momentum transfer ranged from 0.8% to 1.1%, depending on the energy. The uncertainty of the extrapolation factor F was therefore between ±0.22% at the lowest ISR energy and ±0.85% at the highest energy (see Table 8).

vii) *Coulomb corrections ε_C and ε_I.* These corrections amounted to $\sim 7\%$ at the lowest ISR energy and were much smaller at higher energies. The uncertainties of these corrections were due to the indeterminations on the momentum transfer t and on the real part ρ. The uncertainty of t induced an error of ±2% on ε_C and of ±1% on ε_I. Owing to the smallness of ε_C and ε_I, the indetermination of t had a negligible effect. Another small source of error is the uncertainty on the value of the real part ρ, which has recently been measured by the CERN-Rome Collaboration[7]. The values appear in Table 9. It should be noticed, moreover, that in the CR method the value of the total cross-section is less sensitive on ρ at the higher energies. In fact, the derivative of σ, $d\sigma/d\rho \sim \text{const}/t - \rho\sigma$, which is positive at the lowest ISR energies decreases with increasing energy because of the term $1/t$, and can even cross zero for particular values of t and ρ. A summary of the corrections and of the errors induced on σ is given in Table 9.

A summary of all systematic errors affecting the determination of the total cross-section in the CR method is given in Table 10. The statistical error at each energy was between 0.1% and 0.2%. Figure 8 shows all the measurements of F and σ_M performed during the period of data taking. The values finally obtained for σ are summarized in Table 11.

4. LUMINOSITY-INDEPENDENT METHOD

As discussed in the Introduction, if both the elastic and the total rate are measured at the same time in the same intersection, then the luminosity L [$= R_M/\sigma_M$, Eq. (6)] is identical in the two experiments and can be eliminated from Eqs. (7) and (19). In this case the ratio of F [Eq. (19)] to R [Eq. (7)] determines σ without the need for any luminosity measurement:

$$\sigma = \frac{1}{2}\frac{1}{1+\varepsilon}\frac{F}{R}\left[1 + \sqrt{1 - 4\Delta\sigma_{el}\,(1+\varepsilon)\,\frac{R}{F}}\right] . \qquad (27)$$

In order to guarantee the criterion of simultaneous measurements, the triggers for the two experiments were alternatively enabled by the on-line computer at each event. For each ISR run a value of σ was derived using Eq. (27). The averages of the values obtained at each energy are listed in column 4 of Table 12.

The comparison between the values of σ given in Table 12 is interesting in many ways. For instance, the internal consistency of the results is monitored by the ratio λ between the values of σ obtained in the luminosity-independent method and in the PSB method:

$$\lambda = \frac{\sigma(\text{L-ind})}{\sigma(\text{PSB})} . \qquad (28)$$

In the ideal case (no error in any measurement) λ would be equal to 1. Recalling Eqs. (7) and (27) λ can be written to a good approximation as $\lambda \simeq FL/R^2$. Therefore if a scale error affected the luminosity measurements, such as to influence the σ values in the PSB method in a significant manner, then λ would deviate significantly from unity in the same direction at all energies. The results obtained for λ are illustrated in Fig. 9. By averaging over all energies, we obtain

$$\langle\lambda\rangle = 0.9944 \pm 0.0093 , \qquad (29)$$

where the quoted error includes also the systematic uncertainty of ±0.0052 affecting the quantity F which has been discussed in Section 3.4. This result implies that we can guarantee the reliability of the Van der Meer method to about 0.9%. A scale error of ±0.9% on L has therefore been assumed in columns 2 and 3 of Table 12.

Since the absolute scale of the displacements in the Van der Meer method has been independently measured[5], our result can be seen from a different point of view. The consistency between the values of σ obtained in the PSB and in the CR methods can be considered as a proof that, neglecting spin effects, the optical theorem holds true to ±0.5% for proton-proton collisions at ISR energies. This is the most accurate test obtained until now.

5. CONCLUSIONS

Since all methods described above gave consistent results, the three measured quantities R, F, and L were combined with the constraint $\lambda = 1$ in a maximum-likelihood method to find the most probable value of R and F, and then of σ [Eq. (27)]. These maximum-likelihood values of σ are the final values of this experiment and can be found in column 5 of Table 12. They are plotted in Fig. 10 together with previous ISR results (Refs. 1, 2 and 12). At each energy, the agreement between old and new ISR values is as good as could be expected from the quoted

errors. The consistency with the FNAL data[13], shown in Fig. 11 together with lower energy results (Refs. 14 and 15), should also be considered as good, when one takes into account the size of the scale errors attached to both measurements.

The decisive increase of σ observed at ISR energies gives deeper significance to the behaviour of the other hadron-proton total cross-sections, measured thus far only up to the maximum energies available at FNAL ($E_{lab} \simeq 300$ GeV). A panorama emerges where it seems that all hadron-proton cross-sections will continue to increase as $\sqrt{s}$ increases. Several years ago, Cheng and Wu[16] gave theoretical reasons supporting the hypothesis that this high-energy behaviour should be a common feature of all hadron-hadron total cross-sections. For hadron-proton reactions, Lipkin[17] has recently proposed the following "universal" parametrization for $\sigma(Hp)$, the total cross-section of any hadron against protons:

$$\frac{\sigma(Hp)}{mb} = 4.40\ N_q^H\ p_{lab}^{0.13} + 4.00\ N_q^H\ N_{ns}^H\ p_{lab}^{-0.20} + 7.83\left(N_{\bar{d}}^H + 2N_{\bar{u}}^H\right) p_{lab}^{-0.50}\ , \qquad (30)$$

where

N_q^H = total number of quarks and antiquarks in H (= 2 for mesons and 3 for baryons)

N_{ns}^H = total number of non-strange quarks and antiquarks in H

$N_{\bar{d}}^H$ = number of $\bar{d}$ antiquarks in H

$N_{\bar{u}}^H$ = number of $\bar{u}$ antiquarks in H .

The σ measurements presented here are in good agreement with Eq. (30), so we feel justified in presenting in Fig. 11, together with the results of some recent experiments (Refs. 13, 14 and 15), the predictions for the other hadron total cross-sections extended up to $E_{lab} = 10$ TeV.

The confidence with which one can believe that all hadron-proton cross-sections will continue to grow well beyond $\sqrt{s} = 60$ GeV, stems also from considering the results of a recent experiment performed by some of us at the ISR[7], where the ratio ρ between the real and imaginary part of the forward amplitude in pp elastic scattering was measured. It was found that ρ, after crossing zero at $\sqrt{s} \simeq 25$ GeV, continues to grow up to the maximum ISR energy ($\sqrt{s} \simeq 63$ GeV) where it reaches a value of $\simeq 0.10$. Such a large and steady increase implies, through dispersion relations, a vigorous increase of σ well beyond the ISR range, up to at least $\sqrt{s} \gtrsim 200$ GeV corresponding to laboratory energies of ~ 20 TeV, where it is expected to reach a value around 55 mb. It seems unlikely that a phenomenon such as this, covering so great a span of energies, is peculiar to pp interactions.

Acknowledgements

We are indebted to the personnel of the ISR Department, and especially to K. Potter, for their many contributions to this experiment and for the excellent operation of the machine. We are grateful to G. Kantardjian for his co-ordination of technical services and to J. Renaud and M. Wensveen for their supervision during the installation of the apparatus. We are also grateful to M. Busi for much effort in the data reduction, to J. Meyer for helpful discussion, and to J.V. Allaby, W. Duinker, G. Paternoster and M. Romano for help in various phases of the experiment. We thank A. Bechini, R. Donnet and M. Ferrat for their excellent technical support. Thanks are also due to M. Del Colletto and P. Marchi for their skilful mechanical work.

REFERENCES

1) U. Amaldi et al., Phys. Letters 44B, 112 (1973).

2) S.R. Amendolia et al., Phys. Letters 44B, 119 (1973).
S.R. Amendolia et al., Nuovo Cimento 17A, 735 (1973).
G. Bellettini, 5th Internat. Conf. on High-Energy Collisions, Stony Brook, 1973 (ed. C. Quigg) (Amer. Inst. Phys., NY, 1973) AIP Conf. Proc. No. 15; Particles and Fields subseries, No. 7; AEC CONF 730841, p. 9. (The new measurements of the ISR displacement scale indicate that the 1.7% correction adopted in this paper should not be applied.)

3) S. Van der Meer, CERN Internal Report ISR-PO/68-31 (1968).

4) S.R. Amendolia et al., Internat. Conf. on Instrumentation for High-Energy Physics, Frascati, 1973 (Lab. Naz. del CNEN, Frascati, 1973), p. 397.

5) K. Potter, ISR Internal Report (1975).

6) CERN-Pisa-Rome-Stony Brook Collaboration, Phys. Letters 62B, 460 (1976).

7) U. Amaldi et al., Phys. Letters 66B, 390 (1977).

8) U. Amaldi et al., Phys. Letters 36B, 504 (1971).
V. Bartenev et al., Phys. Rev. Letters 31, 1088 (1973).
G. Barbiellini et al., Phys. Letters 39B, 663 (1972).

9) U. Amaldi et al., Phys. Letters 43B, 231 (1973).
V. Bartenev et al., Phys. Rev. Letters 31, 1367 (1973).

10) M.P. Locher, Nuclear Phys. B2, 525 (1967).
G.B. West and D.R. Yennie, Phys. Rev. 172, 1413 (1968).

11) K.M. Terwilliger, Proc. Internat. Conf. on High-Energy Accelerators, CERN, 1959 (CERN, Geneva, 1959), p. 53.

12) K. Eggert et al., Nuclear Phys. B98, 93 (1975).

13) A.S. Carroll et al., Phys. Letters 61B, 303 (1976).

14) S.P. Denisov et al., Phys. Letters 36B, 415, 528 (1971).

15) K.J. Foley et al., Phys. Rev. Letters 19, 857 (1967).

16) H. Cheng and T.T. Wu, Phys. Rev. Letters 24, 1456 (1970).

17) H.J. Lipkin, Phys. Rev. D11, 1827 (1975).

Table 1

VDM calibrations for the monitor ($H_3^L H_4^L H_3^R H_4^R$)

$\sqrt{s}$ (GeV)	σ_M (mb)
23.5	19.70 ± 0.10
30.6	23.15 ± 0.12
44.7	25.76 ± 0.13
52.8	26.15 ± 0.20
62.7	25.74 ± 0.21

Table 2

Comparison of the results obtained with variable and fixed priorities in two TOF sequences, for a typical run at $\sqrt{s}$ = 62.7 GeV

Variable priorities				Fixed priorities			
First TOF sequence	Contrib. (%)	Second TOF sequence	Contrib. (% of total 1)	First TOF sequence	Contrib. (% of total 1)	Second TOF sequence	Contrib. (% of total 1)
H_4-H_4	65.4	TB-TB	21.9	H_4-H_4	65.0	TB-TB	21.8
TB-H_4	4.4	H_4-TB	16.3	TB-H_4	4.2	H_4-TB	16.2
H_4-TB	4.1	TB-H_4	16.5	H_4-TB	4.0	TB-H_4	16.4
TB-TB	16.0	H_4-H_4	35.2	TB-TB	15.9	H_4-H_4	35.2
H_4-H_2	3.7	TB-H_2	1.2	H_4-H_2	3.6	TB-H_2	1.2
TB-H_2	0.3	H_4-H_2	2.7	TB-H_2	0.3	H_4-H_2	2.7
H_2-H_4	3.8	H_2-TB	1.2	H_2-H_4	3.7	H_2-TB	1.2
H_2-TB	0.3	H_2-H_4	2.8	H_2-TB	0.3	H_2-H_4	2.8
H_2-H_2	0.2	H_2-H_2	0.2	H_2-H_2	0.2	H_2-H_2	0.2
H_4-L	1.6	H_4-L	1.8	H_4-L	1.6	H_4-L	1.8
TB-L	0.1	TB-L	0.1	TB-L	0.1	TB-L	0.1
H_2-L	0.1	H_2-L	0.1	H_2-L	0.1	H_2-L	0.1
Total 1	100.0	Total 2	100.0	Total 3	99.0	Total 4	99.7

Table 3

Partial contributions of the various TOFs in typical runs at three different energies

FINAL ANALYSIS Variable priorities	$\sqrt{s}$ = 23.5 GeV Contribution (%)	$\sqrt{s}$ = 44.7 GeV Contribution (%)	$\sqrt{s}$ = 62.7 GeV Contribution (%)
H_4-H_4	52.5	65.2	65.4
TB-H_4	1.9	3.9	4.4
H_4-TB	1.9	3.6	4.1
TB-TB	4.2	11.7	16.0
H_4-H_2	14.0	6.2	3.7
TB-H_2	0.5	0.4	0.3
H_2-H_4	14.0	5.9	3.8
H_2-TB	0.5	0.4	0.3
H_2-H_2	6.4	0.7	0.2
H_4-L	3.0	1.7	1.6
TB-L	0.1	0.1	0.1
H_2-L	1.0	0.2	0.1

Table 4

Summary of the parameters used in the calculation of the correction needed to compensate the loss of elastic events:

$$\frac{d\sigma_{el}}{dt} \propto e^{bt} \quad \text{with } b = b_1 \text{ for } |t| < 0.12 \text{ (GeV/c)}^2 \text{ and } b = b_2 \text{ for } |t| > 0.12 \text{ (GeV/c)}^2$$

$\sqrt{s}$ (GeV)	b_1 $(GeV/c)^{-2}$	b_2 $(GeV/c)^{-2}$	σ_{el} (mb)	Correction (mb)
23.5	11.8 ± 0.2	10.3 ± 0.2	6.77 ± 0.15	0.24 ± 0.03 a)
30.6	12.2 ± 0.2	10.9 ± 0.2	6.93 ± 0.15	0.51 ± 0.04 b)
44.7	12.8 ± 0.2	11.0 ± 0.2	7.20 ± 0.15	1.22 ± 0.07
52.8	13.1 ± 0.2	10.7 ± 0.2	7.43 ± 0.15	1.64 ± 0.09
62.7	13.3 ± 0.2	10.4 ± 0.2	7.57 ± 0.15	2.16 ± 0.12

a) 0.12 mb have been subtracted to balance Coulomb scattering events.

b) 0.07 mb have been subtracted to balance Coulomb scattering events.

Table 5

Correction factors to compensate the loss of inelastic events at small angles

$\sqrt{s}$ (GeV)	Correction (%)
23.5	0.27 ± 0.05
30.6	0.50 ± 0.10
44.7	0.96 ± 0.20
52.8	1.18 ± 0.25
62.7	1.39 ± 0.30

Table 6

Correction factors to compensate for trigger inefficiencies due to dead space

$\sqrt{s}$ (GeV)	Correction (%)
23.5	1.5 ± 0.2
30.6	1.3 ± 0.2
44.7	1.2 ± 0.1
52.8	1.1 ± 0.1
62.7	1.1 ± 0.1

Table 7

Summary of the results obtained with the Pisa-Stony Brook method. The symbols heading columns 3 to 6 are the same as those used in Eq. (7).

ISR energies (GeV)	$\sqrt{s}$ (GeV)	$\sigma_{obs} = \sigma_M(R/R_M)$ (mb)	$\Delta\sigma_{el}$ (mb)	ε (%)	σ(PSB) (mb)
11.8 + 11.8	23.5	37.89 ± 0.23	0.24 ± 0.03	1.77 ± 0.21	38.80 ± 0.25
15.4 + 15.4	30.6	38.86 ± 0.22	0.51 ± 0.04	1.80 ± 0.22	40.07 ± 0.24
22.5 + 22.5	44.7	39.82 ± 0.21	1.22 ± 0.07	2.16 ± 0.22	41.90 ± 0.24
26.6 + 26.6	52.8	40.16 ± 0.31	1.64 ± 0.09	2.27 ± 0.27	42.71 ± 0.35
31.6 + 31.6	62.7	39.81 ± 0.33	2.16 ± 0.12	2.49 ± 0.32	42.96 ± 0.38

Table 8

Extrapolation factors F and their errors

$\sqrt{s}$ (GeV)	$\langle\theta\rangle$ (mrad)	$\langle t\rangle$ 10^{-3} $(GeV/c)^2$	b [a] $(GeV/c)^{-2}$	$F = e^{b\langle t\rangle}$	$\Delta F/F$ (%)
23.5	7.2	7.1	11.8 ± 0.2	1.0875	0.15
30.6	6.6	10.4	12.2 ± 0.2	1.135	0.23
44.7	6.1	18.9	12.8 ± 0.2	1.274	0.44
52.8	5.6	22.1	13.1 ± 0.2	1.336	0.52
62.7	5.1	25.5	13.3 ± 0.2	1.404	0.63

a) Values deduced from the experimental data[8] by means of a linear fit in ln s.

Table 9

Coulomb corrections

$\sqrt{s}$ (GeV)	$\langle t\rangle$ 10^{-3} $(GeV/c)^2$	ρ 10^{-2}	ε_C 10^{-2}	ε_I 10^{-2}	$\Delta\sigma/\sigma$ 10^{-2}
23.5	7.1	0.2 ± 1.5	6.7	-0.8	0.45
30.6	10.4	4.2 ± 1.1	2.9	-1.5	0.15
44.7	18.9	6.2 ± 1.1	0.8	-1.2	0.02
52.8	22.1	7.8 ± 1.0	0.6	-1.2	0.002
62.7	25.5	9.5 ± 1.1	0.4	-1.1	0.02

Table 10

Summary of the systematic errors affecting the determination of σ in the CERN-Rome method

	Point-to-point errors $\Delta\sigma/\sigma$ (%) at $\sqrt{s}$ (in GeV) =					Scale error
	23.5	30.6	44.7	52.8	62.7	$\Delta\sigma/\sigma$ (%)
Luminosity L	0.25	0.25	0.25	0.37	0.41	0.45 a)
Elastic peak PK	0.25	0.25	0.25	0.25	0.25	0.15
Background BG	0.35	0.35	0.35	0.35	0.35	0.15
Border loss BD	0.20	0.55	0.05	0.07	0.15	-
Solid angle $\Delta\omega$	-	-	-	-	-	0.15
Extrapolation $e^{b\|t\|}$	0.08	0.12	0.22	0.26	0.31	-
Real part ρ	0.45	0.15	0.02	0.002	0.02	-
Total $\Delta\sigma/\sigma$ (%)	0.70	0.77	0.55	0.63	0.69	0.52
Total $\Delta\sigma$ (mb)	±0.27	±0.31	±0.23	±0.27	±0.30	±0.22

a) Deduced from the results of Section 4

Table 11

Summary of the results obtained by the CERN-Rome method

ISR energies (GeV)	$\sqrt{s}$ (GeV)	$\langle\|t\|\rangle$ 10^{-3} (GeV/c)^2	$\left.\frac{d\sigma^{el}}{dt}\right\|_{t=\langle t\rangle}$ mb/(GeV/c)^2	$e^{b\langle\|t\|\rangle}$	ρ 10^{-2}	$\varepsilon_C + \varepsilon_I$ 10^{-2}	σ (mb)
11.8 + 11.8	23.5	7.1	75.8 ± 0.8	1.087	0.2 ± 1.5	+5.9	39.01 ± 0.27
15.4 + 15.4	30.6	10.4	74.3 ± 1.1	1.135	4.2 ± 1.1	+1.4	40.38 ± 0.31
22.5 + 22.5	44.7	18.9	68.9 ± 0.7	1.274	6.2 ± 1.1	-0.4	41.45 ± 0.23
26.6 + 26.6	52.8	22.1	68.6 ± 0.8	1.336	7.8 ± 1.0	-0.6	42.38 ± 0.27
31.6 + 31.6	62.7	25.5	67.4 ± 0.8	1.404	9.5 ± 1.1	-0.7	43.07 ± 0.30

Table 12

Total proton-proton cross-sections as a function of the total c.m. energy $\sqrt{s}$. The maximum-likelihood values of the last column are plotted in Fig. 10.

$\sqrt{s}$ (GeV)	σ(PSB) (mb)	σ(CR) (mb)	σ(L-ind) (mb)	σ(maximum-likelihood) (mb)
23.5	38.80 ± 0.25	39.01 ± 0.27	39.22 ± 0.55	38.89 ± 0.21
30.6	40.07 ± 0.24	40.38 ± 0.31	40.55 ± 0.62	40.17 ± 0.21
44.7	41.90 ± 0.24	41.45 ± 0.23	41.00 ± 0.43	41.66 ± 0.19
52.8	42.71 ± 0.35	42.38 ± 0.27	42.02 ± 0.47	42.46 ± 0.26
62.7	42.96 ± 0.38	43.07 ± 0.30	43.20 ± 0.54	43.04 ± 0.29
Scale error	± 0.36	± 0.22	± 0.25	± 0.28

Figure captions

Fig. 1 : General layout of the experiment. Hodoscopes H_1, H_2, H_3, H_4, TB_1, TB_2 in the Left and in the Right arm and hodoscope L detect pp interactions, while hodoscopes A and B measure elastic scattering in the vertical plane.

Fig. 2 : Sketch of the maximum-angle plot used to evaluate the loss of inelastic events at small angles.

Fig. 3 : Inelastic loss at small angles: fits to the maximum-angle distributions in typical runs at three different energies.

Fig. 4 : Time-of-flight distributions of the events satisfying trigger T′, but not trigger T (see Section 2.6.3) in a typical run at $\sqrt{s}$ = = 44.7 GeV. The events plotted in the figure correspond to about 2% of the total number of events, since in this run 142×10^3 beam-beam events satisfying trigger T were recorded.

Fig. 5a : Distribution of hits in hodoscope A when an element of solid angle $\Delta\Omega$ is selected in hodoscope B.

5b : Front view of hodoscope A. The volume of the elastic peak is determined in a fiducial region PK of $7 \times 5 = 35$ elements, centred on the peak itself. The level of inelastic background is evaluated in the regions M and N, which cover about the same θ-interval as the region PK.

Fig. 6 : Illustration of the symbols used in the calculation of the expected number of coincidences between the element (i,j) of hodoscope A and the element (k,ℓ) of hodoscope B.

Fig. 7 : Distribution of the hits in hodoscope A which are in coincidence with hits of the element (7,7) of hodoscope B in a typical run at $\sqrt{s}$ = 52.8 GeV.

Fig. 8 : Directly measured quantities during the whole period of data taking at all energies:

× Ratio of the monitor rate R_M to the quantity F measured in the CERN-Rome method. According to Eq. (19), $\sigma = \sqrt{\sigma_M F/R_M}$.

o Ratio of the monitor rate R_M to the total interaction rate R measured in the Pisa-Stony Brook method.

• Partial cross-section σ_M detected by the monitor $(H_3 \cdot H_4)_L (H_3 \cdot H_4)_R$.

Fig. 9 : Results obtained for the variable λ used to monitor a possible energy-independent scale error in the values of the total cross-section. The quoted errors include the statistical (thin bars) as well as the systematic (thick bars) errors.

Fig. 10 : Results of this experiment shown together with all previous measurements of σ obtained at the ISR (Refs. 1, 2 and 12).

Fig. 11 : Total cross-section data for collisions of p, $\bar{p}$, π^+, π^-, K^+ and K^- against protons at laboratory momenta p_{lab} between 10 and 2000 GeV/c. The curves are computed according to Eq. (30).

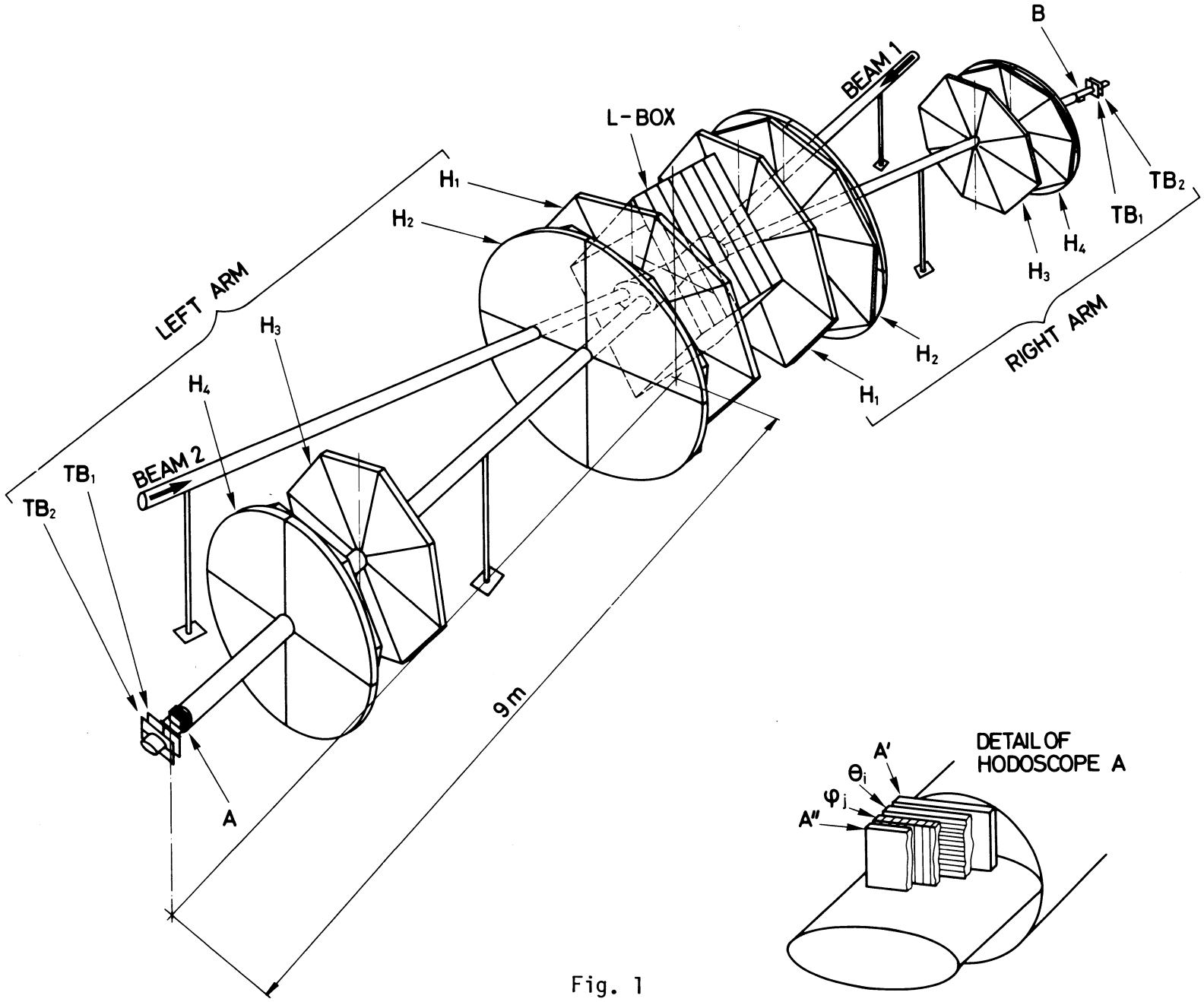
B
BEAM 1
L-BOX
H1
H2
LEFT ARM
H3
H4
BEAM 2
TB1
TB2
A
9m
TB2
TB1
H4
H3
H2
H1
RIGHT ARM
DETAIL OF
HODOSCOPE A
A'
Θi
φj
A''

Fig. 1

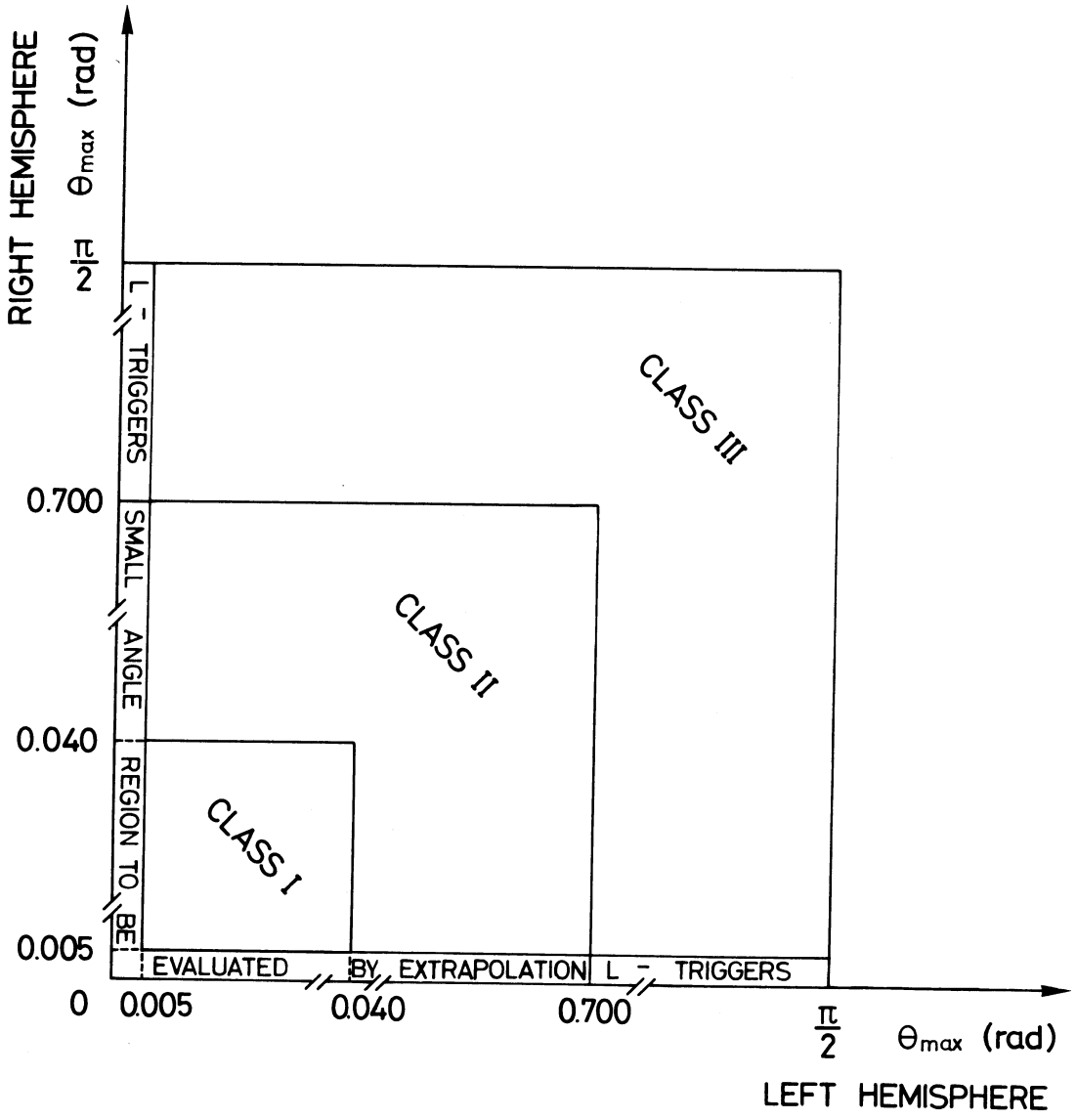
RIGHT HEMISPHERE
θ_{max} (rad)
$\frac{\pi}{2}$
L - TRIGGERS
SMALL ANGLE REGION TO BE EVALUATED BY EXTRAPOLATION
L - TRIGGERS
CLASS III
CLASS II
CLASS I
0.700
0.040
0.005
0
0.005
0.040
0.700
$\frac{\pi}{2}$
θ_{max} (rad)
LEFT HEMISPHERE

Fig. 2

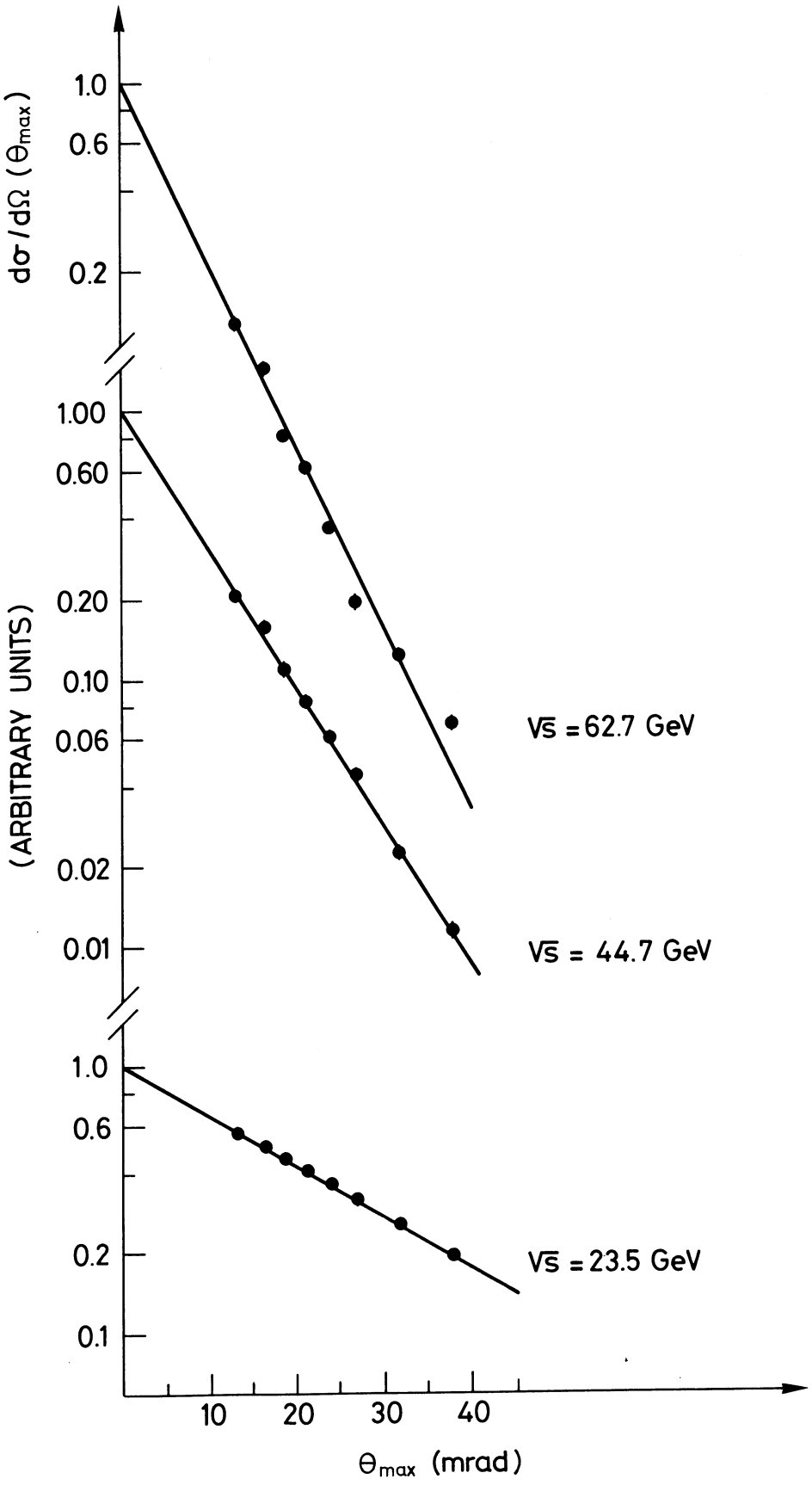
dσ/dΩ (θmax)
1.0
0.6
0.2
1.00
0.60
0.20
0.10
0.06
0.02
0.01
(ARBITRARY UNITS)
√s = 62.7 GeV
√s = 44.7 GeV
1.0
0.6
0.2
0.1
√s = 23.5 GeV
10
20
30
40
θmax (mrad)

Fig. 3

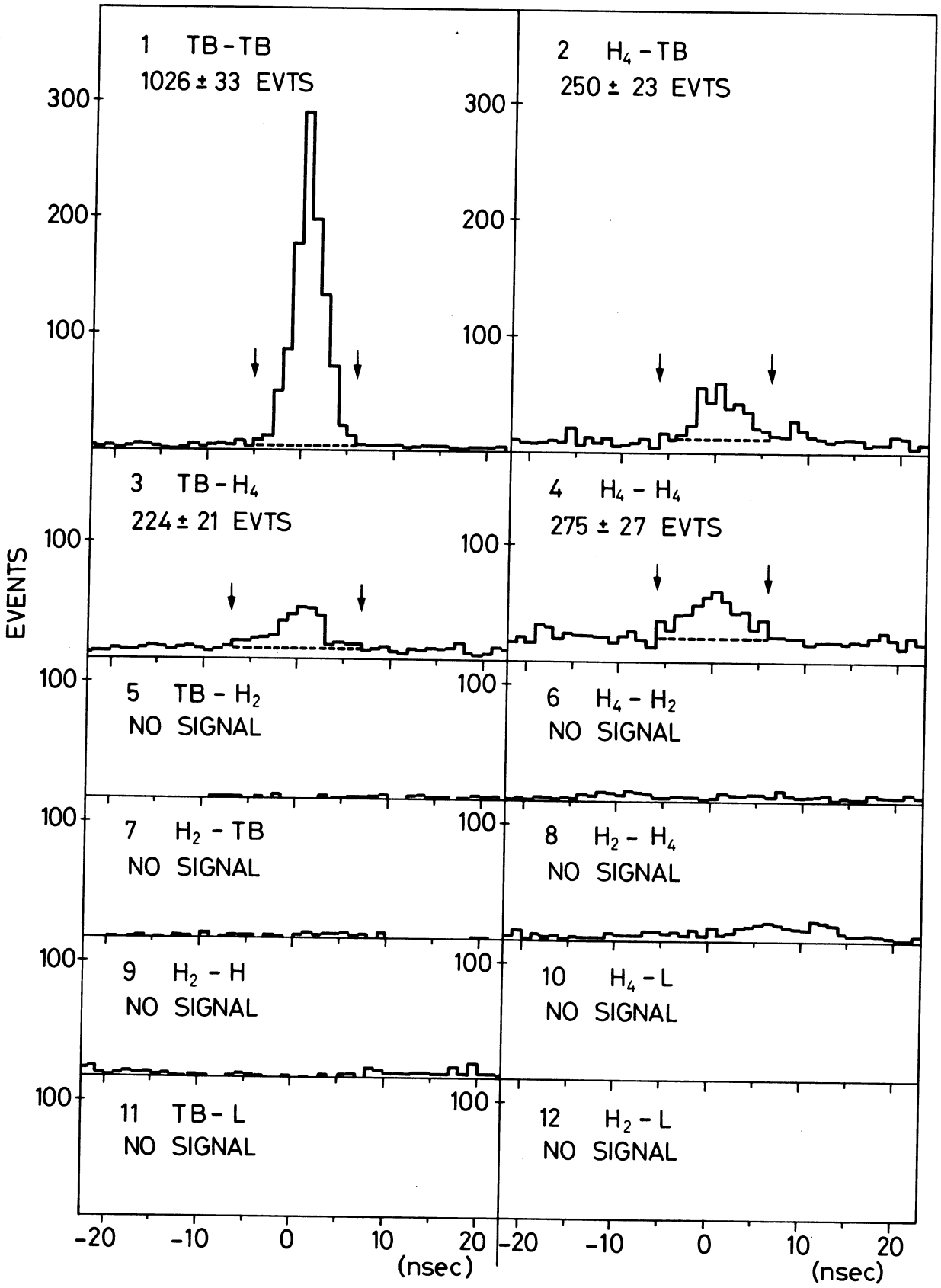
1 TB-TB
1026 ± 33 EVTS
2 H4 - TB
250 ± 23 EVTS
3 TB - H4
224 ± 21 EVTS
4 H4 - H4
275 ± 27 EVTS
5 TB - H2
NO SIGNAL
6 H4 - H2
NO SIGNAL
7 H2 - TB
NO SIGNAL
8 H2 - H4
NO SIGNAL
9 H2 - H
NO SIGNAL
10 H4 - L
NO SIGNAL
11 TB - L
NO SIGNAL
12 H2 - L
NO SIGNAL
EVENTS
300
200
100
-20
-10
0
10
20
(nsec)

Fig. 4

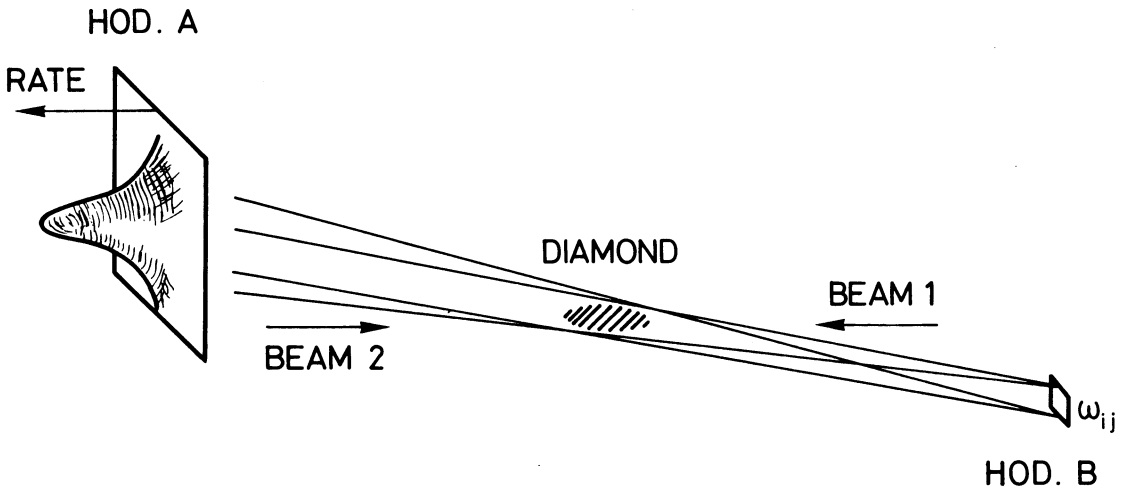
HOD. A
RATE
DIAMOND
BEAM 1
BEAM 2
ω_{ij}
HOD. B

a

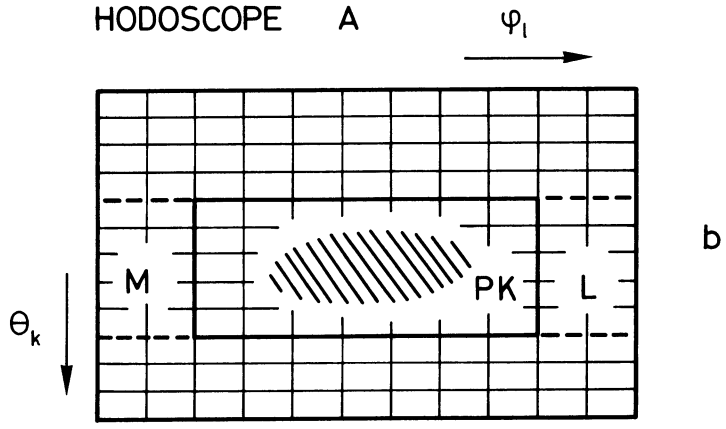
HODOSCOPE A
φ_l
M
PK
L
θ_k

b

Fig. 5

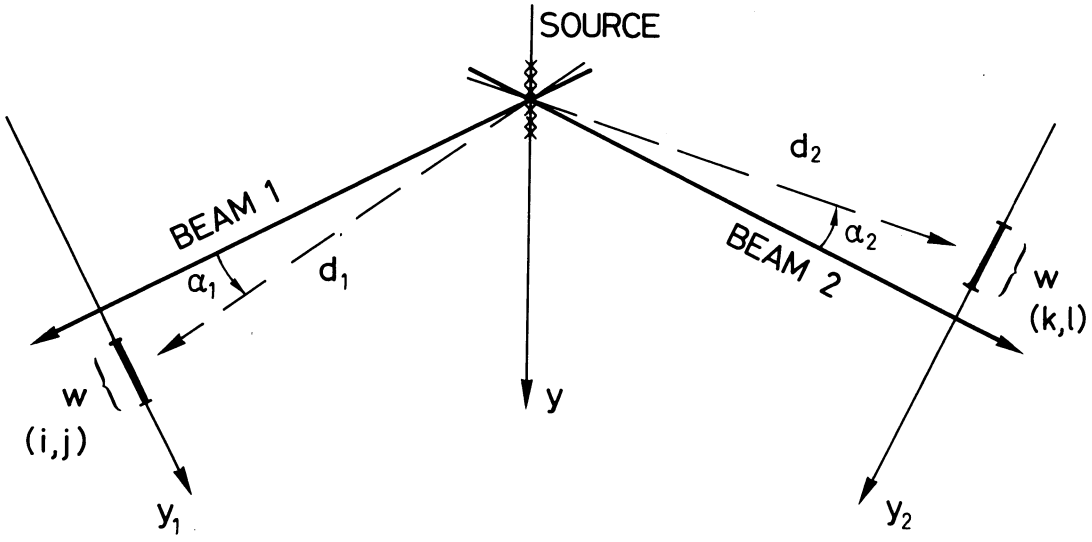

TOP VIEW

SIDE VIEW

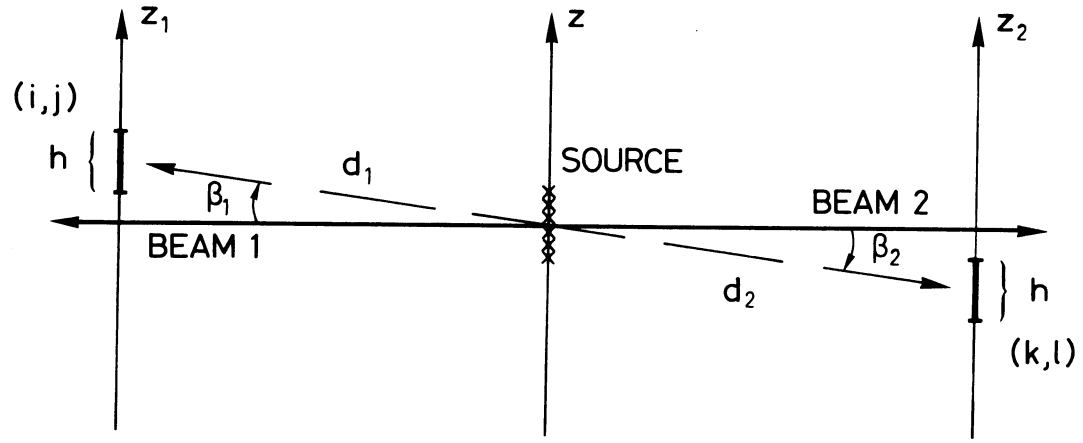

Fig. 6

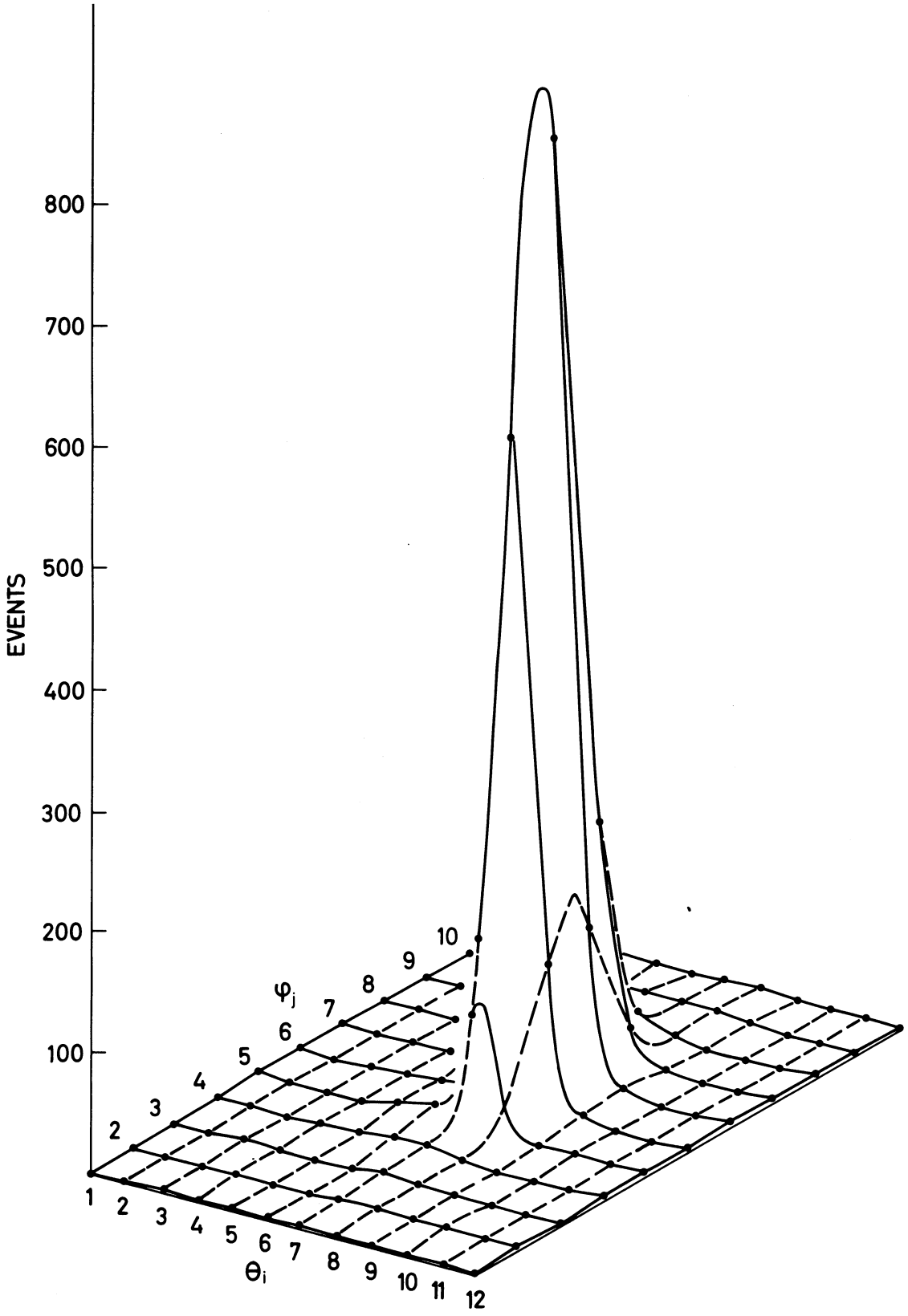
EVENTS
800
700
600
500
400
300
200
100
φ_j
1
2
3
4
5
6
7
8
9
10
Θ_i
1
2
3
4
5
6
7
8
9
10
11
12

Fig. 7

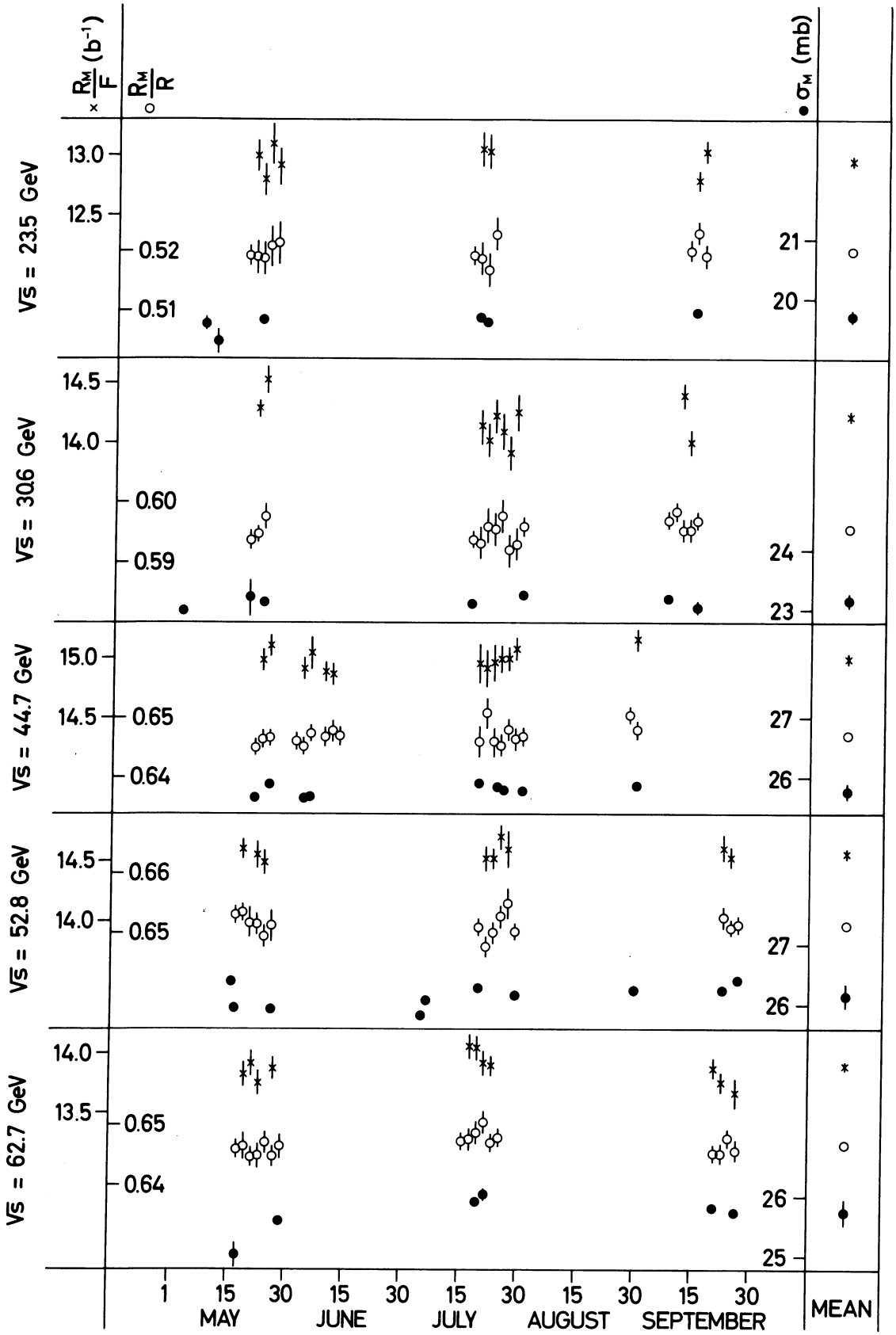
$\frac{R_M}{F}$ (b^{-1})
$\frac{R_M}{R}$
σ_M (mb)
$\sqrt{s}$ = 23.5 GeV
$\sqrt{s}$ = 30.6 GeV
$\sqrt{s}$ = 44.7 GeV
$\sqrt{s}$ = 52.8 GeV
$\sqrt{s}$ = 62.7 GeV
13.0
12.5
0.52
0.51
21
20
14.5
14.0
0.60
0.59
24
23
15.0
14.5
0.65
0.64
27
26
14.5
14.0
0.66
0.65
27
26
14.0
13.5
0.65
0.64
26
25
1
15
30
15
30
15
30
15
30
15
30
MAY
JUNE
JULY
AUGUST
SEPTEMBER
MEAN

Fig. 8

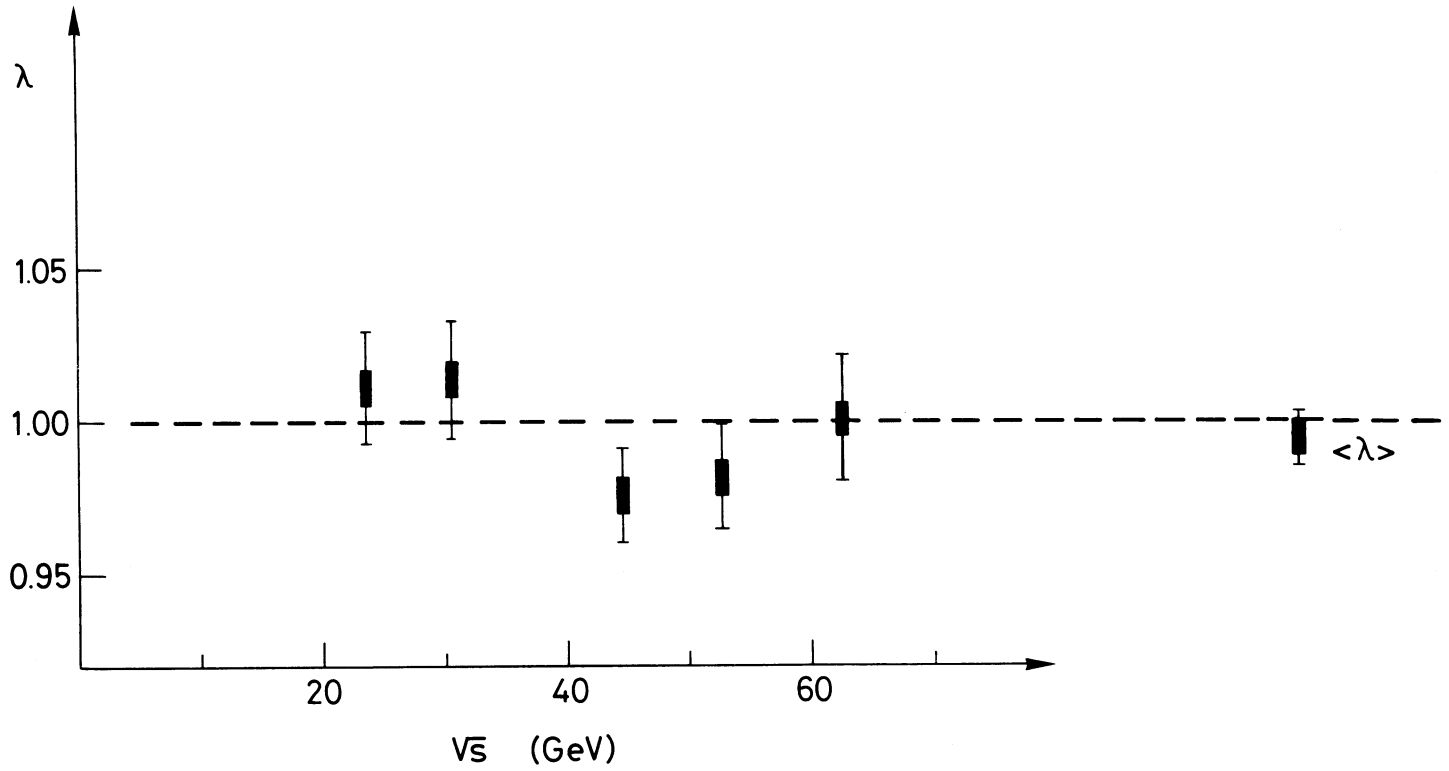

Fig. 9

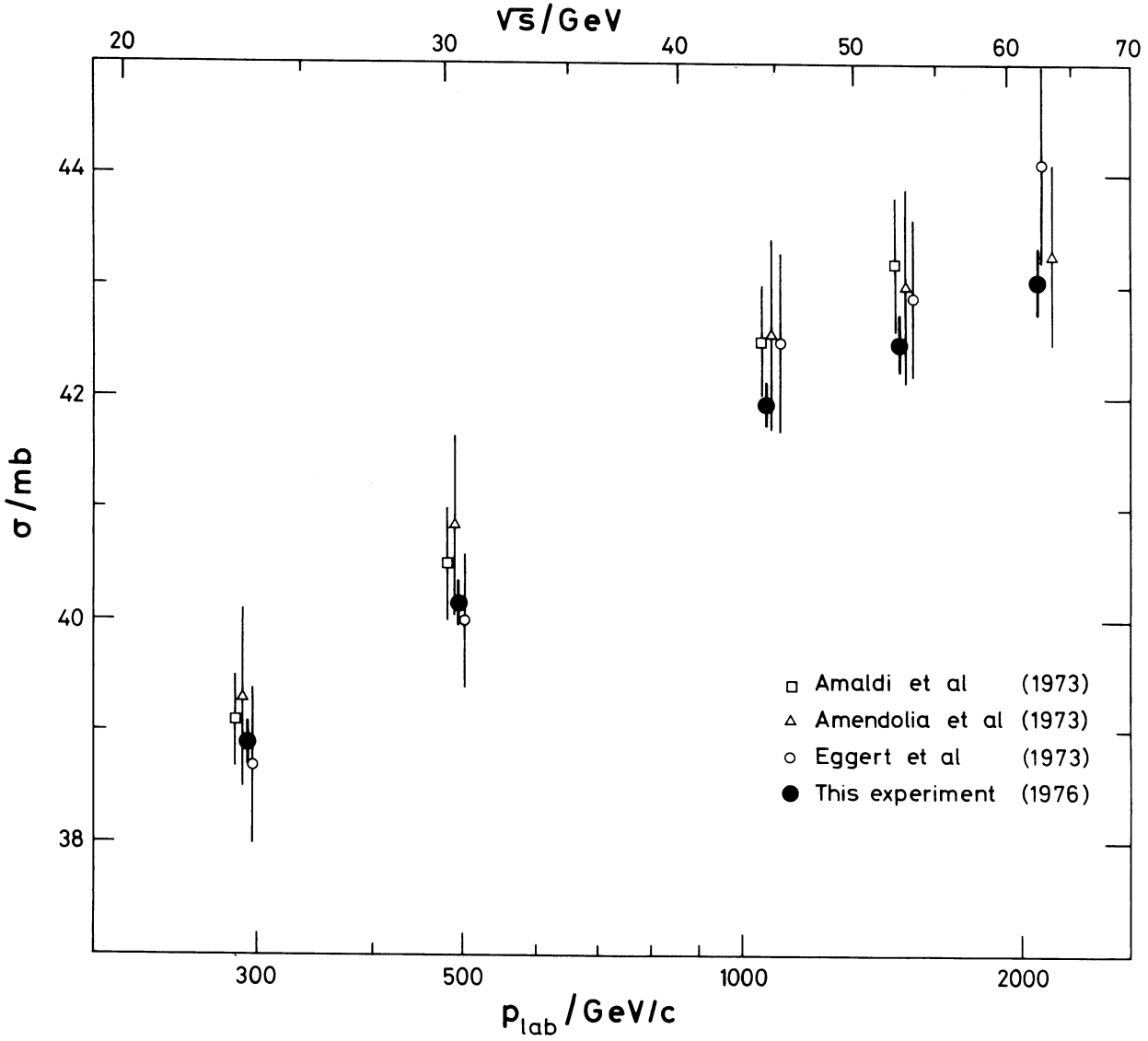
√s / GeV
20
30
40
50
60
70
σ / mb
44
42
40
38
300
500
1000
2000
p_lab / GeV/c
Amaldi et al (1973)
Amendolia et al (1973)
Eggert et al (1973)
This experiment (1976)

Fig. 10

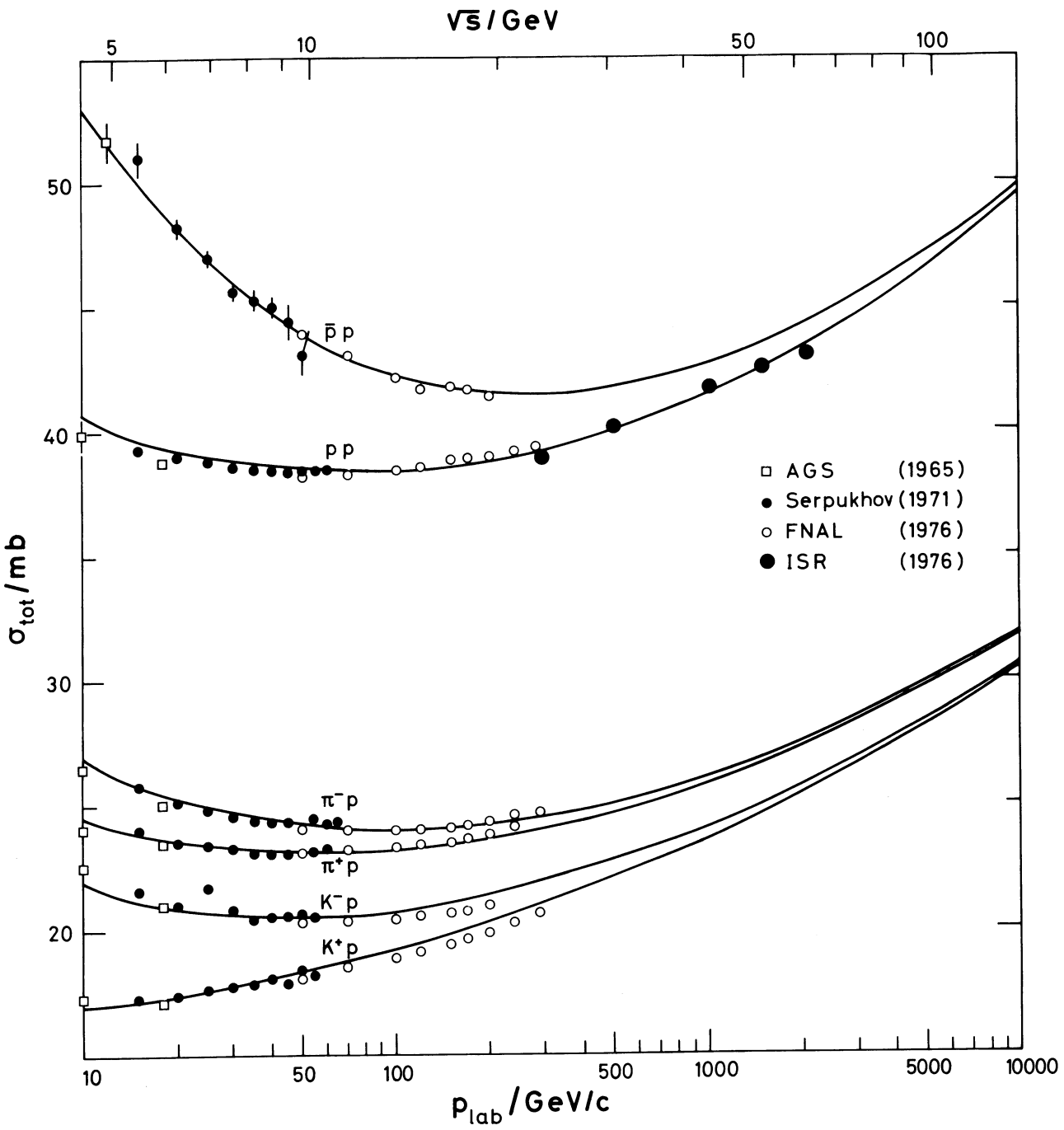
√s / GeV
5
10
50
100
50
40
30
20
σtot / mb
p̄ p
p p
π⁻p
π⁺p
K⁻p
K⁺p
AGS (1965)
Serpukhov (1971)
FNAL (1976)
ISR (1976)
10
50
100
500
1000
5000
10000
plab / GeV/c

Fig. 11